

The worm-LBM, an algorithm for a high number of propagation directions on a lattice Boltzmann grid: the case of phonon transport

René Hammer*, Verena Fritz, Natalia Bedoya-Martínez*

Materials Center Leoben Forschung GmbH, Roseggerstrasse 12, 8700 Leoben, Austria

Abstract

The lattice Boltzmann method (LBM) is a numerical approach to tackle problems described by a Boltzmann type-equation, where time, space, and velocities are discretized to describe scattering and advection. Even though the LBM executes advection along a lattice direction without numerical error, its usage in the high Knudsen number regime (ballistic) has been hindered by the ray effect problem (for dimensions greater than 1D). This problem has its origin in the low number of available propagation directions on standard LBM lattices. Here, to overcome this limitation, we propose the worm-lattice Boltzmann method (worm-LBM), which allows a high number of lattice directions by alternating in time the basic directions described within the next neighbor schemes. Additionally, to overcome the velocity anisotropy issue, which otherwise clearly manifests itself in the ballistic regime (e.g. the $\sqrt{2}$ higher grid velocity of the D2Q8 scheme along the diagonal direction compared to the axial one), the time-adaptive scheme (TAS) is proposed. The TAS method makes use of pausing advection on the grid, allowing to impose not only isotropic propagation but also arbitrary direction-dependent grid velocity. Last but not least, we propose a grid-mean free path (grid-MFP) correction to correctly handle the aforementioned velocity issue in the diffusive limit, without affecting the ballistic one. We provide a detailed description of the TAS method and the worm-LBM algorithm, and verify their numerical accuracy by using several transient diffusive-ballistic phonon transport cases, including different initial and boundary conditions. We demonstrate the accuracy of the new worm-LBM to describe problems where a high angular resolution (i.e. a high number of propagation directions) is required, as the in-plane thermal transport problem under adiabatic-diffusive boundary conditions. In this particular case, we show that schemes with a low number of propagation directions (D2Q8) result in an overestimation of the analytical Fuchs-Sondheimer solution for intermediate and high Knudsen numbers, and that schemes with a higher number of propagation directions are required to correctly describe the problem. Overall, the new, very accurate, and efficient worm-LBM algorithm, free of numerical smearing and false scattering, has the potential to be at the forefront of the numerical solvers to tackle the advective part of different equations in a wide field of applications.

Keywords: Boltzmann transport equation, lattice Boltzmann method, advection solver, diffusive to ballistic, high Knudsen number, phonon transport

1. Introduction

“There is no such thing as a perfect advection scheme - only differing degrees of badness” [1]. The fundamental reason for this is that in any numerical scheme that discretizes space and time, advection does not propagate the field from one lattice site to another but rather interpolates it. This generally leads to numerical dissipation and/or dispersion errors, also known as numerical smearing and angular false scattering. There are many strategies to lower the dispersion error of advection dominated problems within real space schemes [2, 3, 4, 5]. However, a perfect reproduction of the analytical dispersion of the underlying differential equation is only achieved for the

"magic ratio" between time step and grid spacing having a Courant-Friedrichs-Lewy (CFL) number equal to one. This can in general only be fulfilled in 1D (see 1D [6] vs. 3D [7]). A rather inexpensive discretization method that overcomes these problems is the lattice Boltzmann method (LBM). The Lagrangian discretization of the LBM couples velocity and real space exactly. Hence, the CFL number can be chosen to be one for all lattice directions, and advection is reproduced exactly along the lattice. From a practical point of view, an advantage of the LBM is that the discretized field variable (e.g. density) is updated locally in time and space. This makes the LBM efficient and highly parallelizable, such that massive parallel computing architectures with minimal communication requirements and overhead can be used [8, 9]. The LBM has been widely used in fluid dynamics, radiative transfer, neutron transport, rarefied gas dynamics, and phase change

*Corresponding authors: Rene.Hammer@mcl.at, OlgaNatalia.Bedoya-Martinez@mcl.at

[10, 11, 12, 13, 14, 15, 16]. Moreover, it is used in wave propagation, electrodynamics, quantum mechanics, relativistic fluids, ion and electron transport, and diffusive-ballistic phonon transport [17, 18, 19, 20, 21, 22, 23]. The last one, relevant for thermal management at the nano- and micro-scale, is in the focus of the present work.



At length scales comparable to the mean free path of the thermal energy carriers (phonons in the case of semiconductors), or at time scales shorter than their relaxation times, the diffusive picture of heat transport has to be replaced by the so-called ballistic transport [24, 25]. Phonon transport in the ballistic regime is relevant in fields as varied as nano- and micro-electronics, thermal barriers, energy harvesting, nano- and opto-mechanics and quantum technologies [26, 27]. In this regime, as long as the particle nature of the heat carriers prevails, the Boltzmann transport equation (BTE) must be used. The BTE can be used to describe both the continuum (diffusive) and sub-continuum (ballistic) regime. It is routinely used in combination with density functional theory (DFT) calculations to describe bulk phonon transport [28]. However, to account for interface and surface scattering leading to geometrical size effects in thermal transport, it is necessary to solve the time- and space-dependent BTE. This is computationally demanding as it involves seven independent dimensional variables accounting for space, time, and velocity. Monte Carlo (MC) methods have been used traditionally to tackle the high dimensionality issue. However, they are less effective for thermal phonon transport studies, wherein most of the cases one deals with problems close to equilibrium, and small temperature differences have to be tackled accurately. In this case, MC methods spent too much time sampling the equilibrium distribution. This issue has been overcome with the energy-based variance-reduced Monte Carlo formulation [29]. This method is highly efficient, if a linearization of the BTE is justified, and if the superposition principle can be used to propagate the computational particles independently of each other through the system. Nonetheless, it suffers from statistical noise as any MC based technique. For treating temperature-dependent scattering, large thermal gradients, non-equilibrium situations, and in general for obtaining deterministic results, a direct discretization (spatial and angular) of the BTE is desirable. Angular and space discretization can be implemented by combining the discrete ordinates method (DOM) and the finite volume method (FVM) [30, 31, 32, 33]. However, as the advection term in the FVM is not reproduced exactly, numerical smearing and angular false scattering is introduced [30]. This effect is particularly strong if, as frequently done, a simple upwind discretization scheme is used. Recently, the finite-volume based discrete unified gas kinetic scheme (DUGKS) for phonon transport has been proposed [34]. DUGKS makes use of the method of characteristics

instead of the upwind scheme to calculate the convective term.

The LBM is a fully Lagrangian method where advection is performed exactly along the characteristics (as the grid exactly matches the advection) [35]. Despite this favorable property, two severe issues hamper the use of the standard LBM for simulations in the high Knudsen number regime. Firstly, the low number of available propagation directions on the grid introduces a strong ray effect (e.g. 8 for the standard D2Q8 lattice in 2D, Fig. 1a) [36]. Secondly, regular square grids suffer from non-isotropic speed of propagation. For instance, in the D2Q8 lattice the propagation speed along the diagonal directions (directions 5-8, Fig. 1a) is a factor of $\sqrt{2}$ faster than the one along the axial directions (directions 1-4, Fig. 1a). In the framework of the LBM, the 2D grid with the highest number of propagation directions (six directions) with isotropic velocity is the hexagonal D2Q6 (Fig. 1b). The underlying idea of the D2Q6 is that all distances to the next neighbors are equal from each grid point. Extension of this idea to 3D is in principle possible, because Platonic solids fulfill the requirements. Still, the variants are strongly limited because only one Platonic solid, the cube, leads to a completely space-filling tiling of the 3D space [37]. Therefore, the grid with the highest number of propagation directions with isotropic velocity in 3D is the D3Q6. Both the D2Q6 and the D3Q6 are insufficient to overcome the ray effect problem and, hence, are unsuitable for ballistic transport [36]. Other approaches have been proposed to increase the number of propagation directions. For instance, it has been suggested to use enlarged stencils, i.e. high order velocity sets, which propagate among next neighbor lattice points and beyond [38]. Higher-order lattices have also been obtained by discretizing the Boltzmann equation using the roots of Hermite polynomials [39]. The limitation of this method is that the corresponding discrete velocities cannot be incorporated into a regular space-filling lattice. This leads to the loss of the main advantage of the LBM, which is aimed to be used in this work: the exact space discretization of the advection term [40].

In this work, to solve the velocity anisotropy related issue, we propose the time adaptive scheme lattice Boltzmann method (TAS-LBM). The TAS-LBM allows to describe an isotropic speed of propagation on cartesian grids. It can also be extended beyond the isotropic speed of propagation to describe any angle-dependent velocity. Finally, and most importantly, we solve the ray effect issue of the LBM by introducing an arbitrary high (in 2D multiples of 8) number of grid propagation directions, following the approach of Thouy et al. (i.e. propagating among next neighbour lattice points and beyond) [38]. However, to reduce the computational cost and complexity that results from increasing the number of propagation directions [38, 41], we propose the worm-LBM. This method allows to approximate arbitrary directions by alternating in time the basic directions provided by the next neighbor schemes. For convenience, an algorithm allowing schemes

with an arbitrary high number of directions (multiples of 8) is described.

The range of applications for the new worm-LBM, in principle, extends to all transport problems with dominating hyperbolic character. These problems show solutions along characteristics $u(t, \vec{x}) = u_0(\vec{x} - \vec{v}t)$, where u_0 is the initial condition, \vec{x} is space, t is time, and \vec{v} is the velocity. The improvement in the description of the discontinuity properties in hyperbolic problems is of interest for a wide variety of fields of research (see e.g. LeV-*equ* [42] for a comprehensive overview). Here, as it is of high practical relevance, we introduce the new algorithm for solving the BTE, which is a representative example of a first-order transport equation. Note that the BTE is parabolic or hyperbolic depending on the scattering operator. For the Bhatnagar-Gross-Krook operator (BGK), known as the relaxation time approximation [43], the BTE shows a parabolic character and becomes hyperbolic in the limit of weak scattering (i.e. ballistic regime).

In the following, the proposed methods will be explained in detail, and the numerical accuracy will be verified by comparison with analytical solutions in the Fourier and the ballistic limit, using different initial and boundary conditions. Moreover, a comparison to Monte Carlo simulations will be provided for one of the benchmark tests.

2. Models and numerical methods

2.1. Peierls-Boltzmann phonon transport equation

In semiconductors and dielectric materials the phonon contribution to the thermal transport dominates, the electron contribution is negligible, and the heat transport problem reduces to solve the phonon Peierls-BTE. Accordingly:

$$\frac{\partial f}{\partial t} + \vec{v}_g \cdot \nabla f = \left(\frac{\partial f}{\partial t} \right)_{\text{scattering}} \quad (1)$$

where $f(\vec{x}, t, \vec{k}, p)$ is the phonon distribution function of a phonon state (\vec{k}, p) at position \vec{x} and time t . Here, \vec{k} accounts for the wave-vector, and p for the polarization; while \vec{v}_g is the group velocity related to the phonon frequency through the dispersion relation $\vec{v}_g(\vec{k}, p) = \nabla_{\vec{k}} \omega(\vec{k}, p)$. Adopting polar coordinates, the state (\vec{k}, p) can be written as (k, \hat{s}, p) , where $k = |\vec{k}|$ is the wave number and $\hat{s} = (\theta, \phi)$ provides the direction (θ and ϕ are the polar and azimuthal angle, respectively). Thus, using the frequency instead of the wave number, the phonon distribution function is transformed to: $f(\vec{x}, t, \vec{k}, p) \rightarrow f(\vec{x}, t, \hat{s}, \omega, p)$. Note that all variables in Eq. 1 are space and time dependent. In the following, for the sake of clarity, we omit (\vec{x}, t) and use only (\hat{s}, p) as indexes [e.g. $f_{\hat{s}, p}(\omega) = f(\vec{x}, t, \hat{s}, \omega, p)$].

The second term on the left-hand side of Eq. 1 describes the advection of phonons, while the term on the right-hand side denotes the phonon scattering. The latter, in the relaxation time approximation (RTA), can be

written as:

$$\left(\frac{\partial f_{\hat{s}, p}(\omega)}{\partial t} \right)_{\text{scattering}} = \frac{f_{\text{BE}}^{\text{eq}}(\omega, T) - f_{\hat{s}, p}(\omega)}{\tau_{\hat{s}, p}(\omega)}. \quad (2)$$

The RTA assumes that a non-equilibrium phonon distribution function $f_{\hat{s}, p}(\omega)$ relaxes within a time $\tau_{\hat{s}, p}(\omega)$ to the local equilibrium Bose-Einstein distribution:

$$f_{\text{BE}}^{\text{eq}}(\omega, T) = \frac{1}{\exp[\hbar\omega/k_B T] - 1}, \quad (3)$$

where T is the equilibrium temperature, \hbar is the Planck constant divided by 2π , and k_B is the Boltzmann constant. The individual phonon scattering contributions to the relaxation time (i.e. phonon-phonon, phonon-electron, phonon-defect scattering) sum up according to the Matthiessen rule $1/\tau = \sum_i 1/\tau_i$.

Equation 1 can be written in terms of the direction and polarization dependent energy density:

$$\begin{aligned} \frac{\partial e_{\hat{s}, p}(\omega)}{\partial t} + \vec{v}_{\hat{s}, p}(\omega) \cdot \nabla e_{\hat{s}, p}(\omega) \\ = \frac{e^{\text{eq}}(\omega, T) - e_{\hat{s}, p}(\omega)}{\tau_{\hat{s}, p}(\omega)}, \end{aligned} \quad (4)$$

where

$$e_{\hat{s}, p}(\omega) = \int \hbar \omega f_{\hat{s}, p}(\omega) D_{\hat{s}, p}(\omega) d\omega. \quad (5)$$

Here, $D_{\hat{s}, p}(\omega)$ is the direction and polarization dependent phonon density of states per unit volume; and the equilibrium energy density is given by

$$e^{\text{eq}}(\omega, T) = \sum_p \int_{\Omega} \int \hbar \omega f_{\text{BE}}^{\text{eq}}(\omega, T) D_{\hat{s}, p}(\omega) d\omega d\Omega, \quad (6)$$

where $\Omega = \sin \theta d\theta d\phi$ is the solid angle. It is also common to write the BTE in terms of the phonon intensity, which is related to the directional energy density by $I = v_g \cdot e/4\pi$.

Note that the advection term allows for an arbitrary number of propagation directions (\hat{s}), which are coupled by the scattering term. This renders Eq. 4 into an infinite set of coupled differential equations. Therefore, numerical schemes using direct discretization have to include, aside of time and space, angular discretization.

In this work, for simplicity, all the methods are introduced in the framework of the gray approximation. Accordingly, the BTE is solved to predict the distribution function of only one representative phonon mode with average properties (i.e. all phonons have the same polarization, uniform group velocity, and relaxation time). Thus, the density of states can be written as $D(\omega) = 3N\delta(\omega - \omega_0)$, where N is the number of atoms, and ω_0 the phonon frequency. Replacing the density of states into Eq. 6, the equilibrium energy density in the gray model can be written as:

$$e^{\text{eq}}(T) = \frac{3N}{V} \hbar \omega_0 f_{\text{BE}}^{\text{eq}}(\omega_0, T), \quad (7)$$

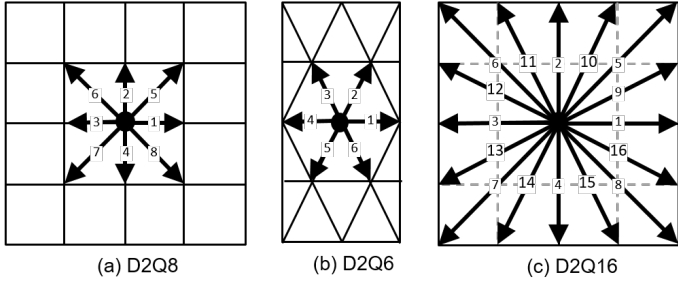


Figure 1: Standard D2Q6, D2Q8 and D2Q16 grids in 2D, with $Q=6, 8$ and 16 propagation directions, respectively.

where V is the unit-cell volume. Nonetheless, all the methods presented here can be straight forward extended to account for an arbitrary phonon band structure. This is known as the dispersion LBM [36, 44]. Alternatively, the "multigray" approach can be also adopted. This method solves multiple uncoupled gray BTEs in parallel, and uses the superposition principle to obtain the final result [45].

2.2. The phonon lattice Boltzmann method

Discretizing the first derivatives in Eq. 4 with respect to time and space:

$$\begin{aligned} \frac{\partial e_{\hat{s}}}{\partial t} &\approx \frac{e_{\hat{s}}(\vec{x}, t + \Delta t) - e_{\hat{s}}(\vec{x}, t)}{\Delta t} \\ \frac{\partial e_{\hat{s}}}{\partial \vec{x}} &\approx \frac{e_{\hat{s}}(\vec{x} + \Delta \vec{x}, t + \Delta t) - e_{\hat{s}}(\vec{x}, t + \Delta t)}{\Delta \vec{x}}, \end{aligned}$$

and introducing angular discretization (i) to account for the phonon propagation in a discrete grid direction \hat{s}_i (see Fig. 1), we define the discrete directional energy density (DDED) e_i . Thus, Eq. 4 can be then written as:

$$\begin{aligned} &\frac{e_i(\vec{x}, t + \Delta t) - e_i(\vec{x}, t)}{\Delta t} + \\ &\vec{v}_{\mathbf{g}i} \frac{e_i(\vec{x} + \Delta \vec{x}_i, t + \Delta t) - e_i(\vec{x}, t + \Delta t)}{\Delta \vec{x}} \\ &= \frac{e_i^{\text{eq}}(\vec{x}, t) - e_i(\vec{x}, t)}{\tau}. \end{aligned} \quad (8)$$

The energy density has to be conserved by the collision operator, i.e. the sum of both sides of Eq. 8, over all grid points has to give a constant value over time. This condition is fulfilled by local equilibrium energy densities calculated as:

$$e^{\text{eq}}(\vec{x}, t) = \sum_i^Q e_i(\vec{x}, t), \quad (9)$$

where the sum runs over all directions Q on the grid. After scattering, the energy is redistributed according to:

$$e_i^{\text{eq}} = \sum_i^Q w_i e^{\text{eq}}(\vec{x}, t), \quad (10)$$

where w_i is an angular weighting factor, with $\sum_i w_i = 1$, accounting for the proportion of solid angle represented by a given direction (see explanation in Sec. 2.4). In simple cases in which the angular space is divided into uniform intervals (e.g. D2Q8, Fig. 1a), and assuming isotropic scattering: $e_i^{\text{eq}} = e^{\text{eq}}/Q$.

In the LBM approach, the space domain is discretized by defining a grid of points separated by a lattice vector $\Delta \vec{x}_i = \vec{c}_i \Delta t$, where \vec{c}_i is a discrete lattice velocity vector. Thus, the energy densities and derived macroscopic quantities are defined at discrete positions on a grid (e.g. in 2D: $\vec{x} = (x_j, y_k)$, with $j, k \in \mathbb{Z}$), and discrete times $t = t_n$ ($n \in \mathbb{N}$). Rearranging Eq. 8, the LBM algorithm can be written as:

$$e_i(\vec{x} + \vec{c}_i \Delta t, t + \Delta t) = (1 - W) e_i(\vec{x}, t) + W e_i^{\text{eq}}(\vec{x}, t). \quad (11)$$

Here,

$$\begin{aligned} W &= \frac{\Delta t}{\tau} = \frac{\Delta x}{v_{\mathbf{g}}} \frac{1}{\tau} = \frac{1}{N} \frac{1}{\text{Kn}} \\ (\Delta x &= \frac{L}{N}, \text{Kn} = \frac{\Lambda}{L}, \Lambda = v_{\mathbf{g}} \tau), \end{aligned} \quad (12)$$

is a weighting factor setting the discrete directional energy density (DDED) (first term RHS of Eq. 11), and the equilibrium energy density (EED) (second term RHS of Eq. 11) contributions. L and N are, respectively, the length of the domain and the number of grid points in which it is divided, Kn denotes the Knudsen number, and λ is the phonon mean free path (MFP). Note that the weight of the scattered term EED decreases with the grid refinement. As the MFP must not change with a finer grid, the DDED has to propagate more grid points per physical length. Hence, less scatter takes place while propagating one lattice spacing. Equation 11 is the core of the LBM method, and it is common to most LBM algorithms.

The local "pseudo" temperature, or also called effective temperature, at a given time (t), and lattice site (\vec{x}) can be calculated by inserting the local equilibrium energy density computed in Eq. 9 into Eq. 7:

$$T(\vec{x}, t, e^{\text{eq}}) = \frac{\hbar \omega_0}{k_{\text{B}} \ln\left(\frac{3N\hbar\omega_0}{V e^{\text{eq}}} + 1\right)}; \quad (13)$$

while the heat flux vector can be calculated according to:

$$\vec{q}(\vec{x}, t) = v_{\mathbf{g}} \sum_i^Q e_i \frac{\vec{c}_i}{|\vec{c}_i|}. \quad (14)$$

Mind that the effective temperature (Eq. 13) provides a comparison between the energy density of a non-equilibrium system and one for which temperature is well defined (i.e. a system at local equilibrium).

2.3. Solving the lattice anisotropy issue: the time adaptive scheme

In the gray approximation, as well as in the isotropic formulation of the dispersive-LBM, a specific phonon mode

travels with the same speed independent of the propagation direction. As discussed in the introduction, Nabovati et.al. [36] have shown that the two dimensional hexagonal scheme D2Q6 (Fig. 1b) provides the grid with the highest number of isotropic lattice vectors. Thus, this grid has the highest number of propagation directions with isotropic speed (six directions). Although this grid is suitable to describe the diffusive regime [36], it poorly describes the ballistic one. The D2Q8, alternatively, resolves two more propagation directions, allows easier handling of the boundary conditions, and provides a natural extension to 3D [23]. However, in this case, the lattice velocity along the diagonal directions is $\sqrt{2}$ times faster than along the axial ones, resulting in an unrealistic phonon propagation [36]. In the diffusive limit (i.e. $\text{Kn} \ll 1$), this velocity error translates into a "grid MFP" $\Lambda_i^{\text{grid}} = \bar{c}_i \tau$ that is a factor of $\sqrt{2}$ longer in the diagonal directions. In this case, a simple solution is to adjust the corresponding τ_i by a factor of $2/(1 + \sqrt{2})$. This correction, however, does not solve the velocity issue in the ballistic limit.

To overcome the problem on regular grids (e.g. the D2Q8) in the ballistic regime, we propose the time adaptive scheme lattice Boltzmann method (TAS-LBM). This method imposes a time condition for the propagation of the DDED's contribution to the LBM, such that phonons are allowed to propagate along the diagonal direction only if they remain within a circle of radius r_{ax} . This radius is given by the distance propagated along the axial directions x_{ax} plus one lattice spacing Δx_i (see Fig. 2). Otherwise, the propagation along the diagonal direction is paused until the condition is fulfilled. The scattering and propagation of the EED part of the LBM is, nonetheless, executed for those directions for which their DDED propagation is paused along the diagonal. In a nutshell, the algorithm for the TAS-LBM can be written as:

$$\text{if } x_{\text{cum}} \leq x_{\text{ax}} + \Delta x_i: \quad (\text{propagating all}) \quad (15)$$

$$e_i(x + \Delta x_i, t + \Delta t) = (1 - W) e_i(x, t) + W e_i^{\text{eq}}(x, t)$$

$$\text{if } x_{\text{cum}} > x_{\text{ax}} + \Delta x_i: \quad (\text{pausing DDEDs})$$

$$e_i(x + \Delta x_i, t + \Delta t) = (1 - W) e_i(x + \Delta x_i, t) + W e_i^{\text{eq}}(x, t),$$

where x_{cum} and x_{ax} are, respectively, the cumulative distances propagated along the direction i , and the axial directions at a certain time step. For the axial directions, the first condition in Eq. 15 is always fulfilled. The upper panel of Fig. 2 shows the hopping evolution during the first five time steps along the D2Q8 grid. As it can be seen, diagonal hopping takes place at time steps $n = 1, 2, 4, 5$, while at $n = 3$ it is paused. As the simulation evolves in time, the distance propagated along the diagonal direction converges toward the distance travelled along the axial axis (lower panel Fig. 2), which over time results in an isotropic speed of propagation. In the limit of $W = 1$, only the evolution of the EED term is contributing, and the algorithm reduces to the standard D2Q8. On the other hand, if W is close to zero, i.e. when the DDED contribu-

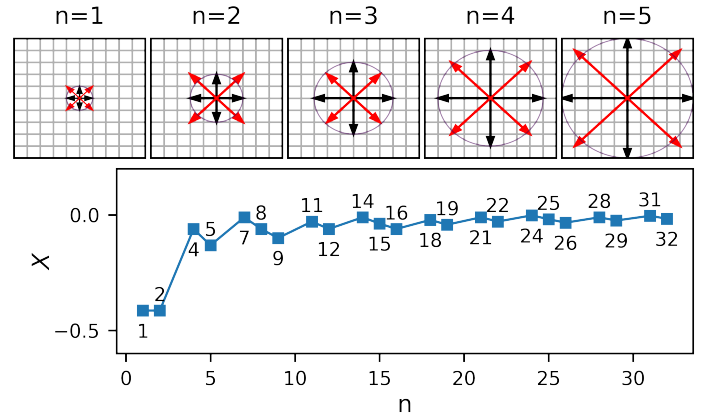


Figure 2: Upper panel: Hopping evolution during the first five time steps along the D2Q8 grid. The arrows indicate the propagation directions and the accumulated distance at each time step n . Lower panel: Relative distance, $X = (\Delta x_{\text{diag}} - \Delta x_{\text{ax}}) / \Delta x_{\text{ax}}$, propagated along the diagonal direction (x_{diag}) with respect to the axial one (x_{ax}) as a function of time n . The numbers within the graphic indicate the time steps n at which diagonal hopping takes place.

tion is dominating, the velocity problem of the standard D2Q8 is repaired by the TAS-D2Q8. Note that values of W lower than one can be cheaply fulfilled in the limit of high Knudsen numbers (ballistic regime), even with a relatively coarse grid ($W = 1/(N\text{Kn})$ see Eq.12). For instance, $W = 0.1$ can be obtained for $\text{Kn} = 1$ using a coarse grid with $N = 10$ grid points.

Special care must be taken when comparing 3D results (analytical or from other numerical methods) to 2D simulations. On the one hand, it should be taken into account that phonons can also move ballistically out of plane in 3D, leading to the following relationship between velocities [36]:

$$v_{\text{g}}^{2\text{D}, \text{effective}} = \frac{1}{\pi} \int_0^\pi v_{\text{g}}^{3\text{D}} \sin \theta d\theta = \frac{2}{\pi} v_{\text{g}}^{3\text{D}}. \quad (16)$$

On the other hand, there is a $2/3$ factor between the diffusivity in 2D and 3D, as can be seen from comparing their corresponding mean square displacements ($\langle \bar{x}^2 \rangle$):

$$\begin{aligned} 2D : \quad \langle x^2 + y^2 \rangle &= 2\langle x^2 \rangle = 2D_2 t \\ 3D : \quad \langle x^2 + y^2 + z^2 \rangle &= 3\langle x^2 \rangle = 2D_3 t \\ &\rightarrow D_2 = 2/3 D_3. \end{aligned} \quad (17)$$

Here D_2 and D_3 are the diffusivity in 2D and 3D, respectively. This effect, as proposed by Guo and Wang [23], can be accounted for by rescaling the lattice velocity with respect to the group velocity (e.g. $c = 2/3 v_g$ for the D2Q8 lattice). They derived this scaling factor by combining the Chapman-Enskog expansion and the Fourier heat equation [23], which in practice consists in adopting the diffusive Fourier limit. The problem of this approach is that it leads to a wrong phonon propagation speed in the transient ballistic regime, where the phonon "wave front" would arrive too late (e.g. $2/3$ slower than the phonon velocity defined

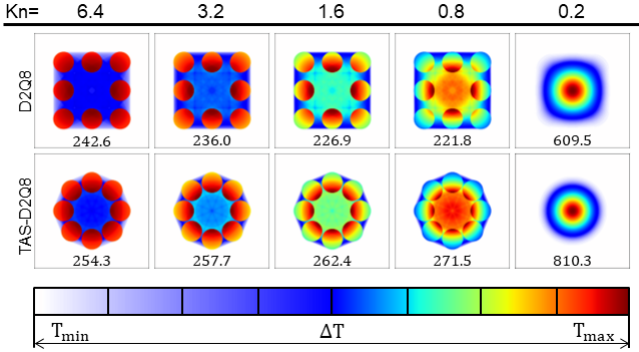


Figure 3: Heat propagation from a circular high-temperature region into a colder infinite domain for five different Knudsen numbers, as obtained with the standard LBM (D2Q8) and the new TAS-LBM (TAS-D2Q8). The initial temperature of the domain, except for a central region of radius $1/11$ of the showed domain length, was set to 299 K. The central region was initialized at 301 K. The total number of grid points was $N = 512$, while the Knudsen number took values of 6.4, 3.2, 1.6, 0.8 and 0.2. The color map starts at the minimum Temperature $T_{\min} = 299$ K (white), and is re-scaled to the highest temperature occurring in the simulation (dark red). The latter is given by the temperature difference $\Delta T = T_{\max} - T_{\min}$ in mK as shown below each sub-figure.

by the group velocity along axial direction, and $2/3\sqrt{2}$ slower in the diagonal one for the D2Q8 grid). In this work, to account for this effect we follow a rather different approach. After setting the grid spacing by computing W according to the desired Knudsen number (see Eq. 12), a new corrected weighting factor W_{corr} is used in the LBM algorithm (Eq. 15):

$$W_{corr} = \frac{3}{2}[(1 - W)W + W(W\Lambda_{corr})], \quad (18)$$

where the $3/2$ factor accounts for diffusivity difference in 2D and 3D (this factor should be used only in those cases in which a 2D simulation is used to emulate a 3D behavior), and

$$\Lambda_{corr} = \frac{2}{1 + \sqrt{2}} \quad (19)$$

accounts for the velocity issue in the diffusive limit for the D2Q8 grid (i.e. different velocities along the axial and diagonal directions). As the correction is done after setting the grid spacing, the velocities are not modified ($\Delta x = v_g \Delta t$). Thus, the correction is applied to the MFPs (by modifying the relaxation times) and not to the velocities. Eq. 18 results as a consequence of mixing the advection of the ballistic non-equilibrium term (first term RHS in Eq. 11), and the transport of the scattered EED term (second term RHS in Eq. 11). The latter has to be corrected since it always propagates as in the standard D2Q8. Thus, in the limit of $W \rightarrow 0$, $W_{corr} = 3/2$, and in the limit of $W \rightarrow 1$, $W_{corr} = 3/2\Lambda_{corr}$.

The performance of the standard (without MFP correction) LBM (D2Q8) and the TAS-D2Q8 is compared in Fig. 3. The heat dissipation from a circular high-temperature region into a colder infinite domain is shown. Five different

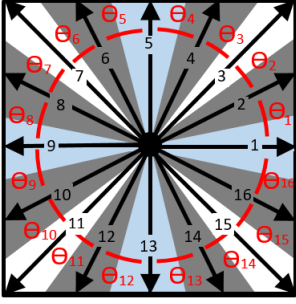
Knudsen numbers encompassing regimes from the ballistic to the diffusive one are considered. The differences between LBM and TAS-LBM are evident in the ballistic regime. Heat propagates faster along the diagonal directions within the D2Q8-LBM scheme, while it propagates isotropically within TAS-LBM. In the diffusive regime, the non-isotropic speed of propagation effect is more subtle. It can be seen, however, that the different contours for the D2Q8-LBM case are more extended than those obtained with the TAS-LBM, as heat is propagated faster. Thus, by the use of a simple time-scheme approach, the TAS-LBM allows to describe a circular propagation on a square grid, making the method particularly suitable for the gray approximation and the isotropic dispersion case. The TAS-LBM, nonetheless, is not restricted to isotropic conditions and can be used to impose any prescribed angle-dependent velocity distribution.

2.4. Solving the ray effect issue, first variant: next-next neighbor advection

In the previous section, we have shown that the TAS-LBM allows isotropic speed of propagation for the advection term on a D2Q8 grid. Nevertheless, as a consequence of the finite number of discrete propagation directions, the angular-dependent temperature profiles feature unrealistic bumps and oscillations as the Knudsen number increases (see temperature profiles in Fig. 3). This problem is known as the ray effect, and it is intrinsic of direct discretization methods [36].

To make the TAS-LBM also accurate in the ballistic regime, it is desirable to have more directions along which the phonons can travel on the grid. The number of directions on a square grid can be augmented by increasing the number of grid points used for advection. For instance, one can resolve eight additional propagation directions for the phonons by advecting to the next-next neighbours in the D2Q8 grid [38] (D2Q16, Fig. 1). In total, there would be 16 directions encompassing three different lattice velocities along the axial (1-4), diagonal (5-8) and, intermediate (9-16) directions. In this case, the TAS-LBM will enable propagation along the diagonal and intermediate directions, as long as the propagated distance is smaller than or equal to the distance traveled along the axial direction at a given time step (i.e. the distance hopped along directions 1-4, Fig. 1). Thus, the TAS-LBM scheme can be easily generalized to enforce a circular propagation for any D2Q $[M \times 8]$ grid, M being an integer. These grids would allow to resolve $M \times 8$ propagation directions, improving the ray effect problem, and providing a more accurate description of phonon transport in the ballistic regime. It is important to remark again that the TAS-LBM goes beyond the isotropic condition, and that it can be used to describe any angular distribution of velocities.

For D2Q $[M \times 8]$ grids with $M > 1$, the angles between adjacent propagation directions get smaller towards the diagonals. To compensate this effect and to take into account the angular interval that should be represented by



D2Q16

$$\Theta_1 = \tan^{-1}(1/2)$$

$$\Theta_2 = \tan^{-1}(2/2) - \Theta_1$$

$$W_1 = (\Theta_0 + \Theta_1) / 4\pi \quad \text{with } \Theta_0 = \Theta_{16}$$

$$W_2 = (\Theta_1 + \Theta_2) / 4\pi$$

$$W_3 = (\Theta_2 + \Theta_3) / 4\pi$$

Figure 4: Example of weight distribution for the D2Q16 grid. Only the weights for the first three directions are listed, the remaining ones can be straightforwardly calculated by using Eq. 21. Note that, $\theta_1 = \theta_4 = \theta_5 = \theta_8 = \theta_9 = \theta_{12} = \theta_{13} = \theta_{16}$, and $\theta_2 = \theta_3 = \theta_6 = \theta_7 = \theta_{10} = \theta_{11} = \theta_{14} = \theta_{15}$.

one direction, an angular weighting function should be introduced. In practice, for a given scheme D2Q[$M \times 8$] there will be a set of $M \times 8$ angles,

$$\theta_j = \tan^{-1}(j/M), \quad (j = 1, \dots, M \times 8), \quad (20)$$

that define $M \times 8$ weight factors:

$$w_j = \frac{\theta_{j-1} + \theta_j}{4\pi} \quad (1 < j < M \times 8), \quad (21)$$

where angular periodic boundary conditions are considered (i.e. $\theta_0 = \theta_{M \times 8}$). An example for D2Q16 grid is provided in Fig. 4. These weight factors are used for the initial and boundary conditions, and for distributing the post-scattering equilibrium energy densities to the different lattice directions (see Eq. 10). Moreover, the grid-MFP correction factor (Eq. 19) has to be generalized for schemes with arbitrary number of Q directions:

$$\Lambda_{corr} = \frac{Q}{\sum_i^Q c_i}. \quad (22)$$

2.5. Solving the ray effect issue, final variant: the worm-LBM

The TAS-LBM provides a reliable approach to correctly describe both the ballistic and the diffusive regimes of phonon transport. Nonetheless, schemes using the next-next neighbor advection (and so forth) have a reduced resolution in space for representing initial conditions, boundary conditions, and inhomogeneities in the material parameters. For instance, while the standard D2Q8 next neighbor advection scheme allows 1×1 structure sizes, the D2Q16 next-next neighbor scheme requires 2×2 structure sizes (i.e. four times more grid points compared to the D2Q8); the D2Q24 next-next-next neighbor scheme requires 3×3 structure sizes (i.e. nine times more grid points), and so forth. Thus, the number of grid points has to increase with the number of directions to keep the space resolution, which increases the computational cost. An

alternative to circumvent this limitation is to encode the spatial propagation in a square grid D2Q[$M \times 8$] (with $M > 1$) into a time adaptive propagation on the D2Q8 scheme (i.e. propagating in time using the directions defined within the D2Q8 next neighbor scheme as building blocks). It can be shown that any propagation direction of a D2Q[$M \times 8$] scheme can be decomposed into the basic directions described within a standard D2Q8 stencil: i.e. using the axial directions 1-4 and the diagonal directions 5-8, as shown in Fig. 5(a). In practice, the diagonal and axial directions of the D2Q8 scheme are repeated in an optimized sequence (worm-path), such that the trajectory in a desired direction is followed as close as possible. The worm-path is repeated every M time steps (worm-sequence time steps), and can be defined at the beginning of the simulation using the following algorithm. Being $l_{Q[M \times 8]}^{\hat{s}}$ the total distance propagated by the advection term after M time-steps in a direction (\hat{s}) within the D2Q[$M \times 8$] scheme, and P_i the nearest neighbour grid point in a direction \hat{i} from the point where advection is taking place, the worm-path finding algorithm reads as:

$$\text{for } \hat{s} = 1, Q = M \times 8 : \quad (23)$$

(loop over the D2Q[$M \times 8$] directions)

for $n = 1, M :$

(loop over the worm-sequence time steps)

$\delta = 1$

for $\hat{i} = 1, 8 :$

(loop over the D2Q8 directions)

$\delta_{i-1} = \delta$

$\delta_i = \text{distance}[l_{Q[M \times 8]}^{\hat{s}} \frac{8n}{M}, P_i]$

if $\delta_i \leq \delta_{i-1} :$

$\delta = \delta_i$

$\hat{r} = \hat{i}$

$K_{\hat{s},n} = \hat{r}$.

Thus, every direction \hat{s} in the D2Q[$M \times 8$] is described by a sequence of M hoppings ($K_{\hat{s},1}, \dots, K_{\hat{s},M}$), where each individual hopping is along one direction \hat{i} selected from the eight basic directions provided by the D2Q8. These are either axial "a" or diagonal "d" directions.

Figure 5(b-e) shows the directions (dotted-dashed lines) and the worm trajectories (dashed arrows) for the worm-D2Q16, worm-D2Q24, worm-D2Q32, and worm-D2Q40 schemes. Similar to the TAS-LBM approach, isotropy is enforced by allowing advection only within a radius given by the distance propagated along the axial directions plus one lattice grid spacing. Conversely, scattering and propagation of the EED contribution is allowed every time step at every lattice site. This method will be, from now on, referred to as the worm-LBM. Note that the worm-LBM reduces to the TAS-LBM in the limit of 8 directions. Thus, for the sake of a unified notation, the TAS-D2Q8 will be

denoted as the worm-D2Q8 in the following. A flowchart illustrating the worm-LBM algorithm is provided in Fig. 6.

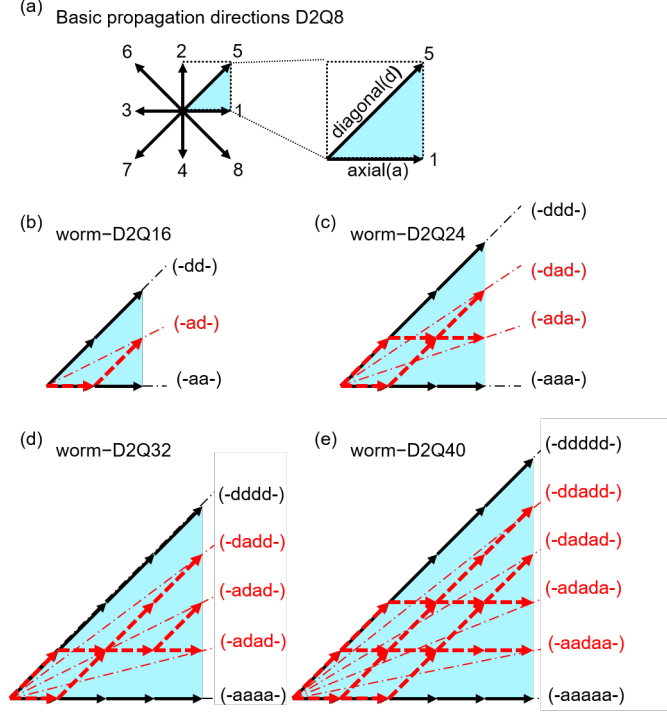


Figure 5: The worm-LBM approach. Propagation on any grid $D2Q[M \times 8]$ is constructed from the basic directions described within the (a) D2Q8 grid. Worm-path examples: (b) worm-D2Q16, (c) worm-D2Q24, (d) worm-D2Q32 and (e) worm-D2Q40. The additionally introduced propagation directions along the $D2Q[M \times 8]$ are described by the dash-dotted lines, while the worm-path composed of axial, a, and diagonal, d, lattice directions are denoted by dashed arrows (listed in round parenthesis). Note that the directions that are not shown in the first quadrant, and on the other three quadrants, are symmetrically equivalent to those depicted.

2.6. LBM boundary treatment

In the following, the boundary treatment for *isotropic blackbody*, *anisotropic phonon radiation*, *adiabatic diffuse*, *adiabatic specular*, and *periodic boundary conditions* is provided. It should be remarked that, even if not explicitly stated for the individual cases, the boundary conditions are also allowed to change their values or character in time.

- *Isotropic blackbody boundary conditions* or, equivalently, isotropic internal blackbody temperature sources at temperature (T). These are imposed by overwriting at every time step the DDEDs (e_i) by the values defined by the desired temperature. In practice, at every time step the EED (e^{eq}) is distributed according to the angular weighting functions introduced in Eq. 21:

$$e_i = w_i e^{eq}(T) \quad \forall i \in [1, Q], \quad (24)$$

where $e^{eq}(T)$ is computed according to a prescribed temperature value T using Eq. 6.

- *Anisotropic phonon radiation boundary conditions* or, equivalently, internal phonon radiation sources. These are imposed by overwriting at every time step the DDEDs (e_i) using a desired radiation distribution $e_{i,imposed}$:

$$e_i = e_{i,imposed} \quad \forall i \in [1, Q]. \quad (25)$$

- *Adiabatic diffuse boundary conditions* or, equivalently, walls with internal diffuse adiabatic scattering. These are generated by updating the DDEDs (e_i) pointing away from the boundary inwards into the domain, by the weighted sum of DDEDs (e_j) pointing towards the boundary:

$$e_i = w_i \sum_j e_j \quad \forall i \in \text{domain inwards}. \quad (26)$$

The sum runs over all DDEDs traveling from the domain towards the boundary.

- *Adiabatic specular boundary conditions* or, equivalently, walls with internal specular adiabatic scattering. These are generated by substituting the DDEDs (e_i) pointing away from the boundary inwards into the domain, by their mirror-like equivalents (e_j) pointing towards the wall, where the mirror plane is the boundary

$$e_i = e_j \quad \forall i \in \text{inwards}, \quad \forall j \in \text{outwards} \quad (27)$$

and $\forall (i, j)$ mirrored pairs.

- *Adiabatic specular-diffusive boundary conditions*. These can be generated as a linear combination of Eqs. 26 and 27.

- *Flux boundary conditions* or, equivalently, walls with internal flux sources. These are generated by imposing a desired flux vector \vec{q} . This boundary condition is not unique, since a specific flux vector can be generated by different combinations of DDEDs. The differences are vanishing in the diffusive limit, but are significant in the ballistic one. Thus, in general, it is recommended to prescribe all the DDEDs uniquely (see "anisotropic phonon radiation boundary conditions"):

$$\vec{q} = v_g \sum_i^Q e_{i,imposed} \frac{\vec{c}_i}{|\vec{c}_i|}, \quad (28)$$

where the sum runs over all Q directions.

- *Periodic boundary conditions*. These are imposed, in 2D, by linking the leftmost to the rightmost, and the lowermost to the uppermost lattice points. For instance, a lattice point sitting on the leftmost boundary receives all directions coming from the right of the lattice point periodically located at the rightmost boundary.

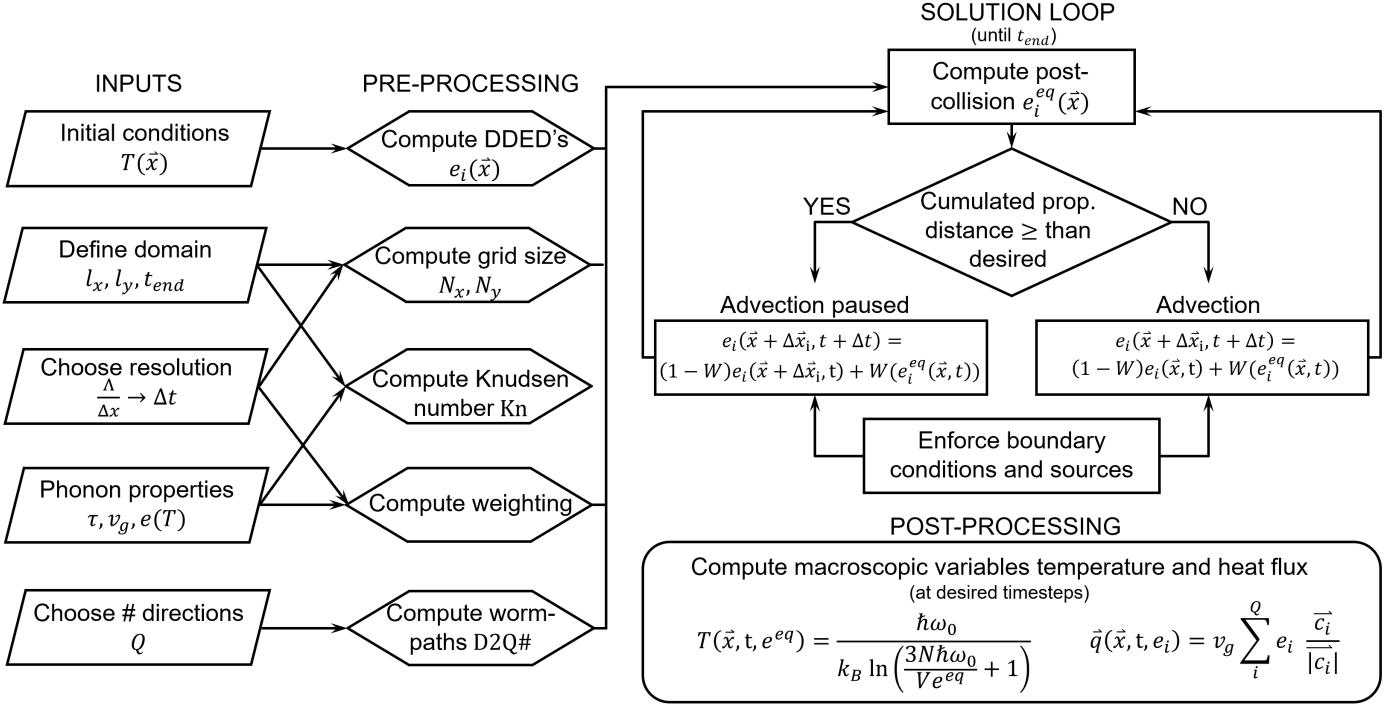


Figure 6: Flowchart of the worm-LBM algorithm

3. Benchmark of the worm-LBM algorithm

In the following, the reliability and accuracy of the worm-LBM algorithm is shown. This is done by comparing the ballistic-diffusive phonon transport problem in 2D to reference solutions (transient and stationary). The latter are either given by analytical solutions, or are obtained from the energy-based variance-reduced Monte Carlo algorithm of Peraud et al. (VRMC) [29] using the program PHONON-CODE [46]. At this point, it should be emphasized that the worm-LBM algorithm has its strength in the intermediate to high Knudsen number regime. Simulations, aiming for a stationary solution at very low Knudsen numbers (diffusive regime), are numerically very expensive. The diffusive regime can be accurately covered by the Fourier heat equation. Here, the simulations in the very low Kn regime are performed mainly to verify the accuracy of the method by using available analytical solutions. The investigated test cases were:

- *The transient "one-pixel source"*, which demonstrates the behavior of the method on the grid scale (Sec. 3.1).
- *The transient of a uniform circular initial condition*, which demonstrates convergence with the number of propagation directions. A comparison to the analytical solution in the ballistic regime is also provided (Sec. 3.2).
- *The transient of a Gaussian initial condition in the Fourier limit*, which is compared to the simple tran-

sient analytical Gaussian solution of the Fourier heat equation (Sec. 3.3).

- *The transient cross-plane heat transport*, which is compared to analytical solutions in the ballistic and Fourier limits, and numerical solutions obtained in the framework of VRMC (Sec. 3.4).
- *The transient in-plane heat transport*, which is compared to the Fuchs-Sondheimer analytical solution for the effective thermal conductivity [47, 48] in the steady limit (Sec. 3.5).
- *The stationary one hot - three cold boundaries test-case*, which is compared to the analytical solution in the Fourier limit (Sec. 3.6).

All simulations were performed in the gray approximation with the phonon properties reported in Tab. 1.

| v_g (m/s) | τ (ps) | λ (nm) | ω (THz) | κ (W/(m K)) | α (cm ² /s) |
|----------------|----------------|-------------------|-------------------|-----------------------|----------------------------------|
| 6400 | 6.53 | 41.792 | 81.8 | 129.998 | 0.892 |

Table 1: Phonon and transport properties used for all the simulations reported in this work (MC and worm-LBM). v_g , τ , λ , ω , κ , and α denote, respectively, group velocity, phonon lifetime, phonon frequency, thermal conductivity, and diffusivity.

3.1. The transient "one-pixel source",

The "one-pixel source" consists of one hot lattice point at temperature (T_{hot}) located at the center of a domain.

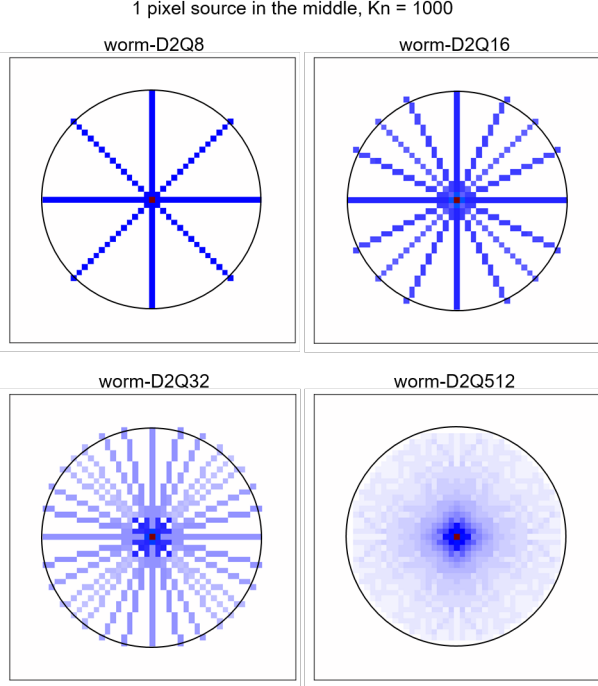


Figure 7: Temperature distribution of "one-pixel source" kept at a constant hot temperature (T_{hot}) in a domain initialized at a uniform lower temperature (T_{cold}). The temperature distribution is visualized after 20 time steps for the worm-D2Q8, worm-D2Q16, worm-D2Q32, and worm-D2Q512. A coarse grid of 51×51 lattice points is used.

The latter is initialized homogeneously at a colder temperature (T_{cold}). The hot lattice point is kept at a constant temperature, using isotropic blackbody boundary conditions. The horizontal and vertical limits of the domain are treated under periodic boundary conditions. A coarse grid (51×51) is chosen to visualize the temperature distribution at the grid level. This test is useful to evaluate the correctness of the advective paths within the worm-LBM schemes, and is highly recommended to test the implementation of the worm-LBM method. As this case is the most challenging in terms of ray effect, numerical smearing, and angular false scattering, it also serves to demonstrate that the worm-LBM algorithm overcomes these problems.

As shown in Fig. 7, the ray effect is reduced by increasing the number of directions, and disappears for the worm-D2Q512 scheme. The number of directions necessary to overcome the ray effect problem depends on the ratio between the source size and the perimeter of the circle depicting the "wave front". Thus, for the extreme case of a one-pixel source, the scheme becomes approximately angular space filling (ASF) if the number of angular directions fulfills $Q_{\text{ASF}} \geq n * 2\pi$, where n is the number of time steps, which are equivalent to the number of propagated lattice grids along the axial directions. This can be generalized for a source of diameter l_{source} , propagating a

distance $l_{\text{propagation}}$:

$$Q_{\text{ASF}} \geq \frac{l_{\text{source}}}{l_{\text{propagation}}} * 2\pi. \quad (29)$$

It is observed, and it is inherent to the worm-LBM algorithm, that the error in the propagation distance (x_i) along a given direction (i) is at maximum one pixel for all times:

$$x_{i,\text{error}} \leq \Delta x_i, \quad (30)$$

i.e. one grid spacing (Δx_i) along the propagation direction. The diagonals would be the directions with the maximum possible error. The axial directions do not show error, since the pausing mechanism introduced in Eq. 15 does not affect them. Thus, they can be used as a reference to estimate the error in the distance propagated along the diagonals (see example in Fig. 2). In general, a maximum deviation of one grid spacing perpendicular to the propagation direction is obtained, in agreement with the algorithm encoded for the worm-paths (see Eq. 23 and Fig. 5).

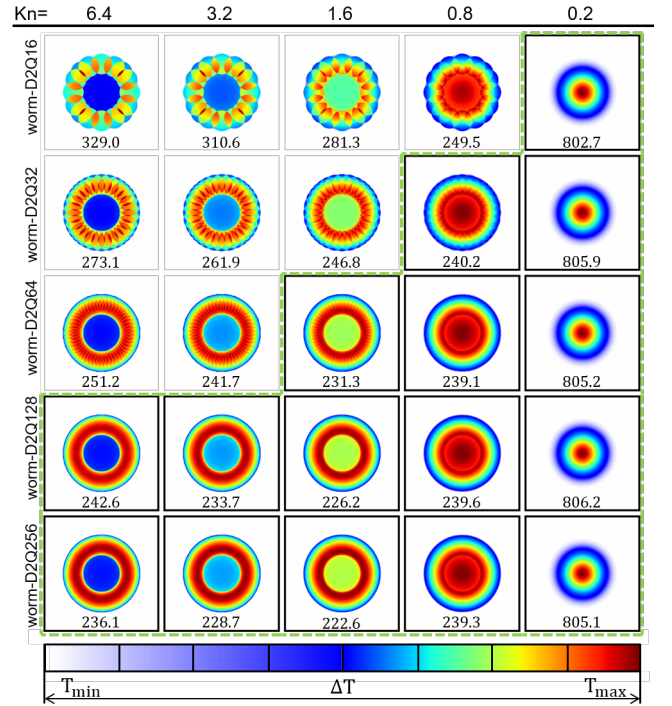


Figure 8: Temperature convergence with the number of directions $Q = 16, 32, 64, 128, 256$, for Knudsen numbers $\text{Kn} = 6.4, 3.2, 1.6, 0.8$ and 0.2 . A grid of size 512×512 lattice points was used for all simulations. A central circular region of the size $1/11$ of the domain size was set at 301 K, while the domain outside of the circle was initialized at 299 K. The results are shown after 127 time steps. The thick-border black boxes framed with green dashed lines highlight the converged simulations, taking as a criterion a relative error threshold of 3% with respect to the solution with the highest number of directions (i.e. the D2Q256). The color map starts at the minimum Temperature $T_{\text{min}} = 299$ K (white), and is re-scaled to the highest temperature occurring in the simulation (dark red). The latter is given by the temperature difference $\Delta T = T_{\text{max}} - T_{\text{min}}$ in mK as shown below each sub-figure.

3.2. The transient of a uniform circular initial condition

Although the transient uniform circular source condition is related to the "one-pixel" problem studied before, it is more practical and closer to a real physical situation. Here, a hot circular initial condition with uniform temperature $T_{\text{hot}} = 301$ K and radius $1/11$ of the domain size is initialized in a uniform cold background at $T_{\text{cold}} = 299$ K. Periodic boundary conditions are imposed on the horizontal and vertical edges of the domain (see Sec. 2.6). This test case is used to quantify the convergence with the number of propagation directions for Knudsen numbers in the ballistic and diffusive regime. As shown in Fig. 8, due to the ray effect, the solution does not converge for a too low number of lattice directions. The thick-border black boxes, framed by green dashed lines, highlight the simulations that are within 3 % of the error for the highest temperature in the domain. The error is calculated, taking as reference the solution obtained with the worm-D2Q256 scheme, which has the highest number of propagation directions among the schemes considered. It can be seen that higher Knudsen numbers require much more directions to reach convergence.

In this particular case, it is straight forward to derive an analytical solution for the resulting intensity profile in the ballistic limit. The intensity (or temperature) along the x -axis can be computed by the circle equation $(x - v_g t)^2 + y^2 = R^2$, weighting it by the circle density $1/x$, where x is the distance propagated from the midpoint. Since the problem fulfills rotational symmetry, the solution can be written for an arbitrary direction as:

$$T(r, t) = \frac{T}{\pi} \frac{\sqrt{R^2 - (r - v_g t)^2}}{r}, \quad (31)$$

where $r = |\vec{r}|$ is the distance from the midpoint.

Figure 9 shows a comparison to the analytical solution for the temperature distribution obtained with the worm-D2Q256 scheme, and $\text{Kn} = 100$. The solution is reported after propagating 192 time steps (i.e. $t \approx 65.3$ fs). The influence of the angular discretization is still slightly visible for this very high Knudsen number case. A stepped appearance in the temperature profile can be seen by zooming into the profile (lower-panel Fig. 9).

3.3. The transient of a Gaussian initial condition in the Fourier limit

In this test case, the worm-LBM is compared to the 2D analytical solution for the temperature distribution of a Gaussian initial condition in the Fourier limit. The analytical solution for the temperature, as derived from the heat equation, is [49]:

$$T(x, y, t) = \frac{4\sqrt{\alpha t_0}}{\sqrt{\alpha(t_0 + t)}} e^{-\frac{(x-x_0)^2 + (y-y_0)^2}{4\sqrt{\alpha(t_0 + t)}}}, \quad (32)$$

with $t_0 = \sigma_0^2/(2k)$. Here, σ_0 is the initial width defined in terms of the Gaussian standard deviation, and α is

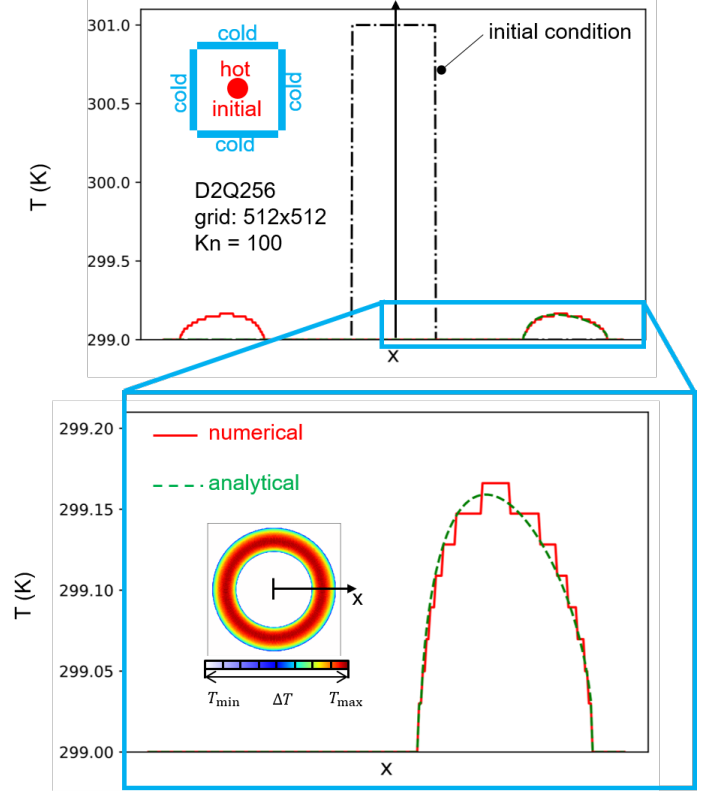


Figure 9: Temperature profile of a uniform circular initial condition: comparison of the worm-D2Q256 algorithm to the analytical solution in the ballistic limit ($\text{Kn} = 100$). A hot circular initial condition at $T_{\text{hot}} = 301$ K and radius $1/11$ of domain size, is initialized in a uniform cold background at $T_{\text{cold}} = 299$ K (dot-dashed black line). The solution is shown after 192 time steps (red and green curves), which corresponds to $t \approx 65.3$ fs. A grid with 512×512 lattice points was used. The temperature profile was calculated along the x direction for $y = Ny/2$. The inset in the lower panel shows the temperature distribution at $t \approx 65.3$ fs.

the phonon thermal diffusivity. Figure 10 shows the grid convergence of the worm-D2Q8, worm-D2Q16 and worm-D2Q64 schemes for a Gaussian initial condition, and $\text{Kn} = 0.005$. A first-order convergence rate is observed, and the coarser grid in all cases shows errors below 0.004 % with respect to the solution obtained with the finest grid considered. As a high number of directions is not necessary in the diffusive limit, the worm-D2Q8 is already in excellent agreement with the analytical solution (Fig. 11).

| x_0 (nm) | y_0 (nm) | σ_0 | k (cm^2/s) |
|------------|------------|------------|--------------------------------|
| 5567.63 | 5567.63 | 556.76 | 0.89 |

Table 2: Parameters for the Gaussian initial distribution (Eq. 32) used in our simulations.

3.4. The transient cross-plane heat transport

The transient cross-plane heat transport corresponds to a 1D problem with periodic boundary conditions perpendicular to the heat flux (see Fig. 15a). Isotropic black-body boundary conditions with temperatures $T_h = 300.5$

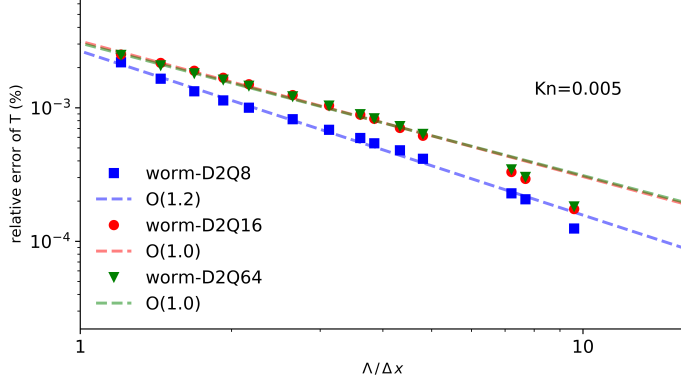


Figure 10: Grid convergence of the worm-D2Q8, worm-D2Q16 and worm-D2Q64 schemes for a Gaussian initial condition, and $\text{Kn}=0.005$. The temperature value in the middle of the domain (hottest point) is compared to the value obtained with the finest grid calculated ($\lambda/\Delta x = 14.4$). The data correspond to time $t = 195.9\tau \approx 1279$ ps. The dashed lines represent different convergence tendencies obtained from fitting the numerical data. Table 2 list the parameters used for the Gaussian initial distribution (Eq. 32).

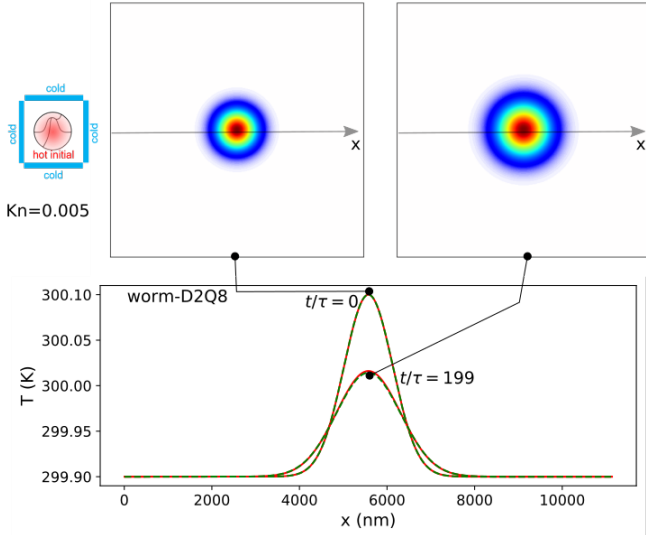


Figure 11: Comparison of the transient temperature profiles obtained with the worm-D2Q8 (red solid line) to the analytical solution (green dashed line) for a Gaussian initial condition (black dash dotted line). The temperature profile corresponds to $t = 199.8\tau \approx 1305$ ps, and $\text{Kn} = 0.005$. Moderately fine grid resolution was used, such that $1/W = \tau/\Delta t = \text{MFP}/\Delta x = 6$ ($N_x \times N_y = 1600 \times 1600$). Table 2 list the parameters used for the Gaussian initial distribution (Eq. 32). The temperature profiles were calculated along the x direction for $y = N_y/2$. The upper panels show the temperature distributions in the entire domain at different time steps.

K and $T_c = 300$ K are imposed on the left and right walls, respectively. The domain is initialized at $T_c = 300$ K.

In the diffusive limit ($\text{Kn} \ll 1$), the temperature and heat flux distributions are compared to the analytical solutions [23]:

$$\Theta(X, \xi) = \quad (33)$$

$$1 - X = \frac{2}{\pi} \sum_{l=1}^{\infty} \frac{1}{l} \sin(l\pi X) \exp\left(-\text{Kn} \frac{l^2 \pi^2 \xi}{3}\right)$$

and

$$Q_x(X, \xi) = 1 + 2 \sum_{l=1}^{\infty} \frac{1}{l} \cos(l\pi X) \exp\left(-\text{Kn} \frac{l^2 \pi^2 \xi}{3}\right), \quad (34)$$

with

$$X = \frac{x}{L}, \quad \xi = \frac{t}{\tau} \text{Kn}, \quad \Theta = \frac{T - T_c}{T_h - T_c} \quad (35)$$

$$\text{and } Q_x = \frac{qL}{\kappa(T_c - T_h)}.$$

Here, L is the non-normalized domain length in the heat flux direction, and q is the magnitude of the non-normalized heat flux. As it can be seen in Fig. 12, the transient and the steady states of the cross-plane heat transport problem in the Fourier limit are perfectly described by the new worm-LBM algorithm. There is a nearly perfect agreement between the worm-LBM results, the analytical solutions and the MC results.

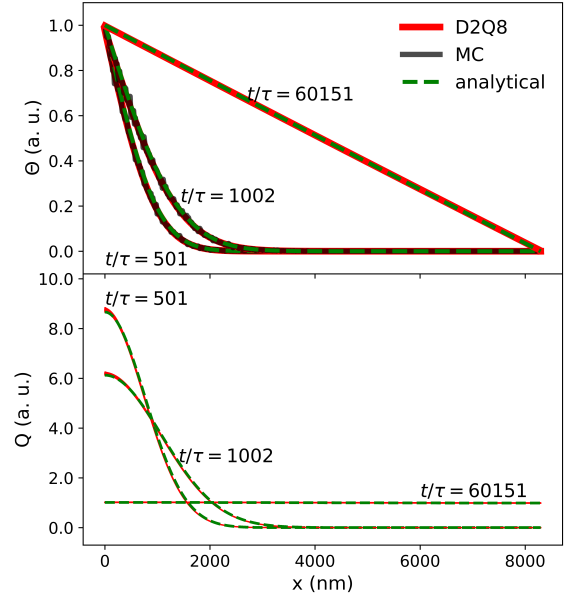


Figure 12: Fourier cross-plane temperature and heat profiles predicted by the worm-D2Q8 algorithm compared to the analytical solutions (Eqs. 34 and 34). The MC results were calculated using the PHONON-CODE [46]. $T_h = 300.5$ K, $T_c = 300.0$ K, $N_x = 12670$, $N_y = 1$, $\text{Kn}=0.005$, $1/W \approx 63.8$. At every time step, t/τ , reported in the lower-panel, heat fluxes for $t/\tau \pm 10$ are shown. The transient MC simulations were performed using 5000000 particles, 50000 maximum number of scattering events, and a grid of 500×1 detectors (see details about the parameters in [46]). The steady MC was not calculated for this Knudsen number.

The worm-algorithm by pausing the advection of the DDEDs along the diagonal directions, while continuing propagation the EED, introduces small fluctuations in time for the energy. The impact of such fluctuations is negligible for the effective temperature (upper-panel Fig. 13). Still, they can result in variations of the heat flux of the

order of 10 % for a very coarse grid (lower-panel Fig. 13). Nonetheless, the amplitude of such fluctuations, and hence the error of the heat flux, reduces with the grid size (lower-panel Fig. 13). In practice, a good estimator of the heat flux is an average value (e.g. over 10 time steps) around the desired time. As it can be seen in the example of Fig. 12, where the heat flux for ten time steps around the desired times are reported, the fluctuation of the heat flux is small for a well grid converged system. In the following, all heat flux data reported or used to calculate another quantity (e.g. thermal conductivity) is averaged over ten time steps around the time of interest.

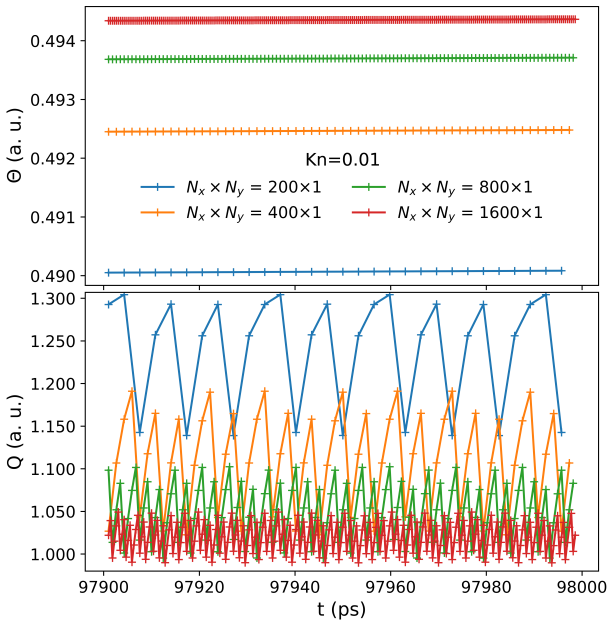


Figure 13: Time evolution of the effective temperature and heat flux of the cross-plane heat transport at the center of the domain ($N_x/2$) close to the steady state. As values are normalized according to Eq. 36, and are reported close to the steady state, the heat flux and temperature converges with the grid size toward 1 and 0.5, respectively.

In the ballistic limit ($Kn \gg 1$), the temperature distribution can be computed analytically by combining the discrete energy density coming from the wall, e_{T_W} , and the isotropic contribution defined by the initial condition e_{T_0} . T_W and T_0 are, respectively, the wall and initial temperature conditions. At a given time, only discrete energy densities from a distance $R = v_g t$ can reach a point located at a distance x to the wall (Fig. 15b). This point will be reached only by energy densities emitted by the wall within the angular interval $(-\theta_W, \theta_W)$, with $\theta_W = \arccos x/R$. Thus, the total equilibrium energy density can be written as:

$$\begin{aligned} e^{eq} &= 2 \left[\int_0^{\theta_W} e_{T_W} d\Theta + \int_{\theta_W}^{\pi} e_{T_0} d\Theta \right] \\ &= 2\pi e_{T_0} + 2\Theta_W [e_{T_W} - e_{T_0}], \end{aligned} \quad (36)$$

and the temperature can be computed using Eq. 13. Fig.

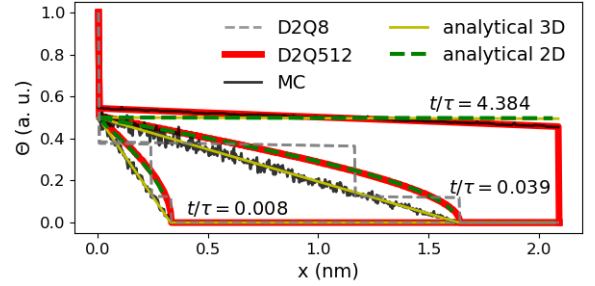


Figure 14: Ballistic cross-plane temperature profile predicted by the worm-D2Q512 algorithm compared to the analytical solution (Eq. 36). $N_x = 510$, $N_y = 1$, $Kn=20$, and $1/W \approx 10225$. The transient and steady MC simulations were performed using 9000000 particles, 90000 maximum number of scattering events, and a grid of 500×1 detectors (see details about the parameters in [46]).

14 shows a comparison of the worm-D2Q512 solutions to the 2D analytical ones (Eq. 36), and to results obtained with MC. The MC result gives a linear "wave front" profile as opposed to the other two solutions (2D analytical and worm-D2Q512), which show a temperature profile which is dominated by the arccos function. Nonetheless, in the limit of long simulation times (once the wave front reaches the left wall) all solutions converge toward the same steady state (e.g. Fig. 14 $t/\tau = 4.384$). The difference in the transient regime has its origin in the dimensionality of the problem. Although the code used in our MC simulations solves the BTE in 2D [46], the total equilibrium energy density is calculated considering the solid angle (Fig. 15c) to emulate the 3D behavior [29]. Thus, the MC temperature profile follows the corresponding 3D analytical solution (Fig. 14).

For the sake of comparison, Fig. 14 includes the temperature profile provided by the worm-D2Q8. As can be seen, such a reduced number of propagation directions in the ballistic regime results in a very bad resolution for the temperature distribution.

In this test-case, as in the Gaussian initial condition, a first-order convergence rate is observed (Fig. 16). This demonstrates that the order of convergence is preserved in the presence of the applied boundary conditions.

From a practical point of view, it is relevant to compute the effective 1D cross-plane thermal conductivity for different Knudsen numbers. Figure 17 shows a comparison of the worm-D2Q8 thermal conductivities to the analytical solutions provided by Hua et.al. [50] and Guo et.al. [23]. In the entire range of Knudsen numbers, the worm-LBM provides solutions in agreement with the analytical solutions. For low Knudsen numbers, the effective thermal conductivity converges to the bulk thermal conductivity. In practice, the worm-LBM should be used at intermediate and high Knudsen numbers, whereas it is sufficient and computationally more efficient to solve the Fourier heat equation for low Knudsen number dominated problems.

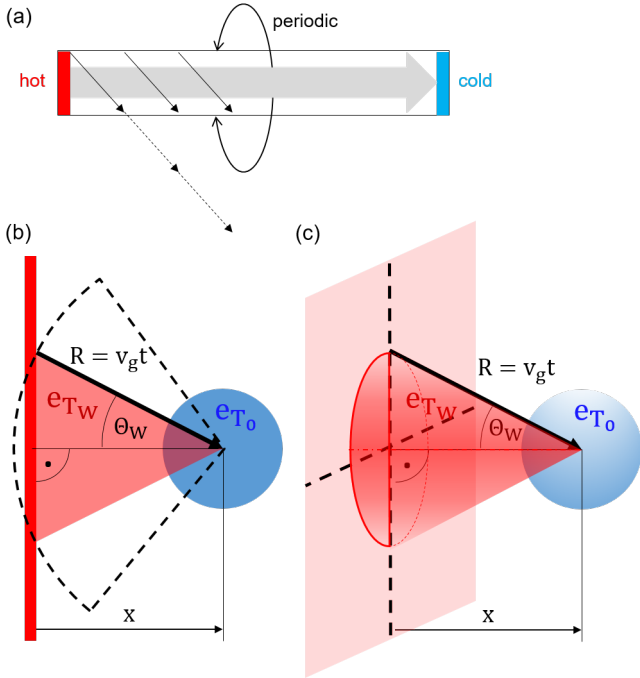


Figure 15: (a) Schematic of the cross-plane test case. (a) Planar angle in 2D, and (c) solid angle in 3D measured from a point located at a distance x to the wall.

3.5. The transient in-plane heat transport

The transient in-plane and cross-plane heat transport problems are very similar to each other. The difference relies on the type of boundary condition applied perpendicular to the main heat flux direction, which in this case is adiabatic-diffuse (see Sec. 2.6). Moreover, the Knudsen number is defined by the width of the domain, instead of the distance between the hot and cold walls. All the other parameters are kept equal, i.e. isotropic blackbody boundary conditions for the left ($T_h = 300.5$) and right ($T_c = 300$) walls, and uniform initial domain temperature ($T_c = 300$ K). After reaching steady state, the numerical solutions for the in-plane thermal conductivity are compared to the Fuchs-Sondheimer analytical expression [23].

Figure 18 shows the convergence in terms of the number of directions (Q-convergence) of the in-plane thermal conductivity in the ballistic and diffusive regimes, taking as a reference the values predicted by the worm-D2Q128 scheme. In the limit of very low Knudsen numbers (diffusive limit) the worm-D2Q8 scheme is reasonably well converged, with errors of $\sim 12\%$ with respect to the worm-D2Q128 value. Conversely, for high Knudsen numbers the worm-D2Q8 value is much higher than the result obtained with the worm-D2Q128 ($\sim 260\%$). In the D2Q8 scheme, there are just three directions (two diagonals and one axial) available to propagate the energy along the heat flux direction, and a large proportion of the energy is propagated along the axial direction, without being affected by the boundary scattering. As the number of directions increases, more and more energy is propagated along di-

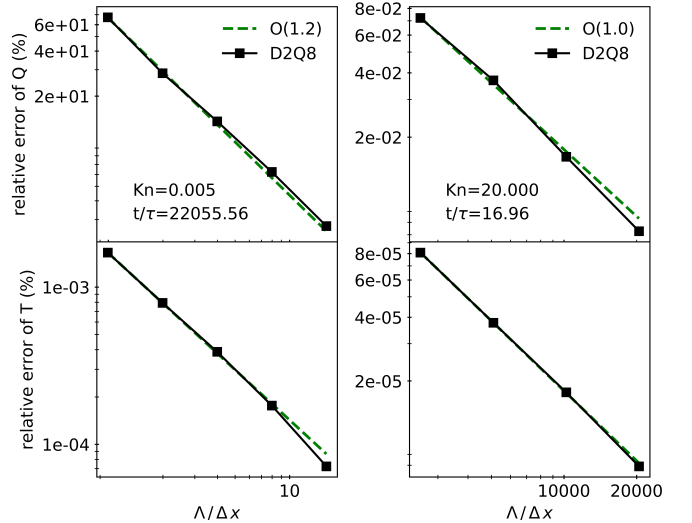


Figure 16: Grid convergence for the transient cross-plane temperature profile. Left panel: $Kn = 0.005$. Right panel: $Kn = 20$. The temperature and heat flux over the entire domain at a given time-step is averaged and compared to the numerical solution of the finest grid. The finest used grids were $\lambda/\Delta x \sim 64$ ($Kn = 0.005$), and $\lambda/\Delta x = 81900$ ($Kn = 20$).

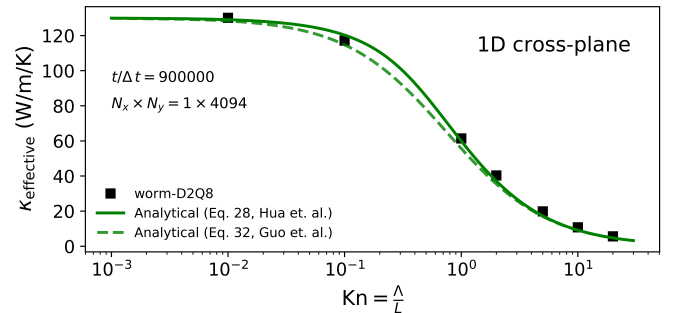


Figure 17: Knudsen number dependence of the 1D cross-plane thermal conductivity at 300.25 K. Analytical solutions were taken from Hua et.al. [50], and Guo et.al. [23].

rections for which boundary scattering becomes possible.

Figure 19 shows the grid convergence tendency for the in-plane transient effective thermal conductivity, taking as a reference the value obtained with the finest grid. Here again, a first-order convergence rate is observed.

An important parameter to correctly estimate the in-plane thermal transport in the ballistic regime is the domain length-width ratio. This parameter is independent of the numerical algorithm for solving the BTE, and has to be considered in any case. In the limit of high Knudsen numbers, one should ensure large ratios to avoid constraints of the phonons mean free path by the hot and the cold walls. Here, for the highest Knudsen number considered, a ratio of $N_x/N_y = 16.79$ underestimates the value obtained with $N_x/N_y = 134.68$ by $\sim 18\%$ (lower-panel Fig. 20). Conversely, in the diffusive limit differences below 1% are obtained. The small differences among different N_x/N_y ratios in this case have origin on

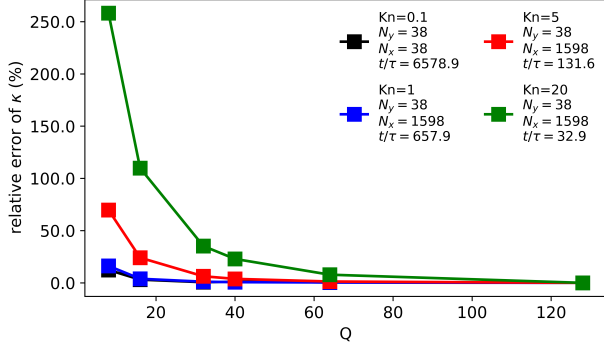


Figure 18: Number of directions convergence (Q -convergence) of the in-plane thermal conductivity, taking as reference the value obtained with the worm-D2Q128 scheme.

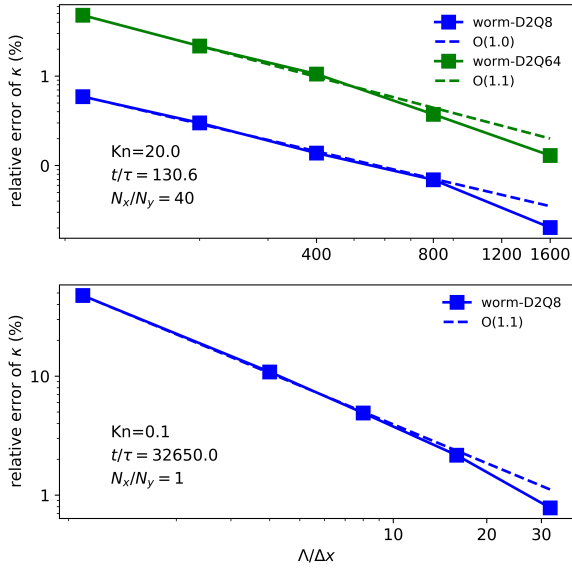


Figure 19: Grid convergence of the in-plane transient thermal conductivity, using as reference the value calculated with the finest grid (i.e. $\lambda/\Delta x = 3200$ for $\text{Kn} = 20$, and $\lambda/\Delta x = 64$ for $\text{Kn} = 0.1$, respectively).

the time step at which the solution is computed and compared (see Fig. 20), which have not been large enough to fully reach the steady state. Simulation times were chosen following a linear dependence with the length-width ratio, $t/\tau = 5000 * (N_x + 2)/(N_y + 2)$, which is not fulfilled in the diffusive regime.

Taking into account the convergence tests in terms of number of directions, grid size, and length-width ratios, the Knudsen number dependence of the in-plane effective thermal conductivity was compared to the analytical solution (Fig. 21). As it can be seen, LBM schemes with high number of propagation directions are necessary to correctly describe the in-plane thermal conductivity in the ballistic regime. The standard scheme with only eight directions results in a considerable overestimation of the analytical solution (e.g. 307 % for $\text{Kn}=20$). As explained before, the problem has its origin in a too large propor-

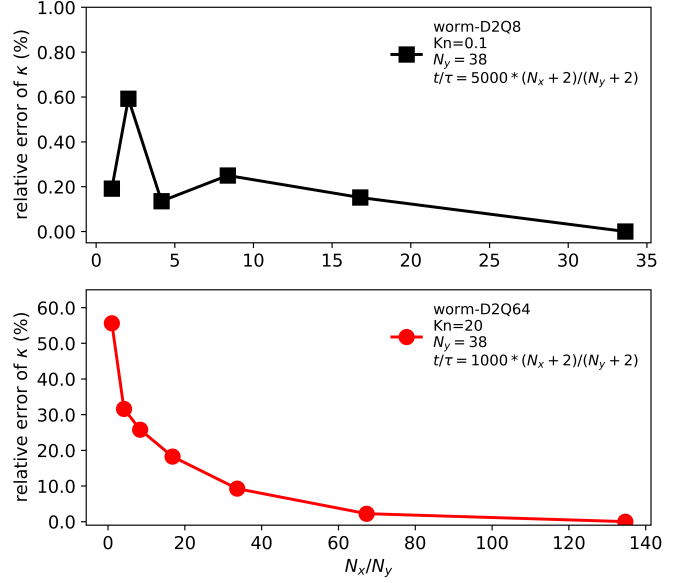


Figure 20: Domain length convergence of the in-plane transient thermal conductivity. k_{ref} is the value calculated with the largest domain. The domain length corresponds to the distance between the cold and hot walls (i.e. $N_x \times \Delta x$), where the grid space Δx is defined from the domain width $N_y = 38$.

tion of energy propagating along the axial direction, which never interacts with the adiabatic diffuse wall. The worm-LBM naturally remedies the problem by allowing more propagation directions, without having to resort in fitting procedures to the analytical solution as previously proposed by other authors [23]. As it can be seen in Fig. 21, the numerical solution converges with the number of propagation directions toward the analytical value. For the intermediate and low Knudsen numbers ($\text{Kn} = 0.1, 1, 5$), the effective thermal conductivity does not change further for $Q > 40$. Conversely, for $\text{Kn}=20$, the values calculated with $Q=128$ and $Q=256$ still differ in around $\sim 4\%$. In all cases, finer grids would be necessary to obtain a better agreement with the analytical solution. Here we have omitted such grid convergence, as the main objective of this test case was to show the impact of the propagation directions.

3.6. The stationary one hot - three cold boundaries

The one hot - three cold boundary condition problem consists of four isotropic blackbody walls at temperatures $T_h = 300.5$ K (upper wall) and $T_c = 299.5$ K (remaining walls). A Knudsen number of $\text{Kn} = 0.005$ is imposed for the propagation from the upper to the lower wall. In the diffusive limit, the temperature and heat flux profiles in the steady state along the X direction at different Y heights were calculated with the worm-D2Q8 scheme (Fig. 22), and compared to the analytical solutions:

$$\Theta(X, Y) = \sum_{l=1}^{\infty} \frac{2[1 - \cos(l\pi)]}{l\pi \sinh(l\pi)} \sin(l\pi X) \sinh(l\pi Y), \quad (37)$$

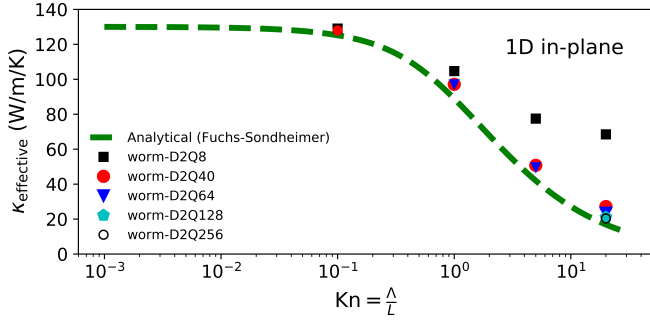


Figure 21: Knudsen number dependence of the 1D in-plane thermal conductivity at 300.25 K. The data correspond to: $N_x \times N_y = 318 \times 318$, and $t/\Delta t = 160000$ ($\text{Kn}=0.1$); $N_x \times N_y = 5118 \times 38$, and $t/\Delta t = 256000$ ($\text{Kn}=1, 5$). For $\text{Kn}=20$ the data corresponds to $t/\Delta t = 64000$. The numbers reported inside the graph correspond to the error in percentage of the worm-LBM numerical solution, taking as reference the analytical value.

$$Q_x(X, Y) = - \sum_{l=1}^{\infty} \frac{2[1 - \cos(l\pi)]}{\sinh(l\pi)} \cos(l\pi X) \sinh(l\pi Y), \quad (38)$$

$$Q_y(X, Y) = - \sum_{l=1}^{\infty} \frac{2[1 - \cos(l\pi)]}{\sinh(l\pi)} \sin(l\pi X) \cosh(l\pi Y), \quad (39)$$

with $X = \frac{x}{L}$ and $Y = \frac{y}{L}$. Overall, the heat flux and temperature profiles within the domain match the analytical Fourier solution very well. However, the agreement gets reduced as the distance to the hot boundary becomes smaller (e.g. $0.97l_y$). Close to this boundary, the transport problem becomes more ballistic, and the Fourier solution is not valid anymore. Consistently, we found that schemes with a low number of propagation directions (e.g. D2Q8) are less accurate than higher-direction schemes in the vicinity of the hot boundary, and particularly close to the corners where ballistic transport dominates. Figure 23 shows a comparison of the transient heat flux as obtained with different worm-D2QM ($M=8, 32, 64$, and 128) schemes. In regions where diffusive transport dominates, the numerical solution is independent of the number of propagation directions (i.e. Q), while it becomes dependent in the ballistic areas. The impact of the number of propagation directions is, of course, higher as the entire domain becomes dominated by ballistic transport. In the limit of high Knudsen numbers ($\text{Kn} = 1$ and 10), schemes with a too low number of propagation directions (e.g. $Q = 8$ and 16) suffer much more from the ray effect problem than domains dominated by small Knudsen numbers ($\text{Kn} = 0.1$), see Fig. 24.

A clear difference between the transport character of this problem in the ballistic and diffusive regime can be seen from comparing the temperature profiles for different Knudsen numbers (Fig. 25). As the Knudsen number increases, a temperature slip at the limits of the domain is observed. The larger the jump, the more the ballistic transport dominates.

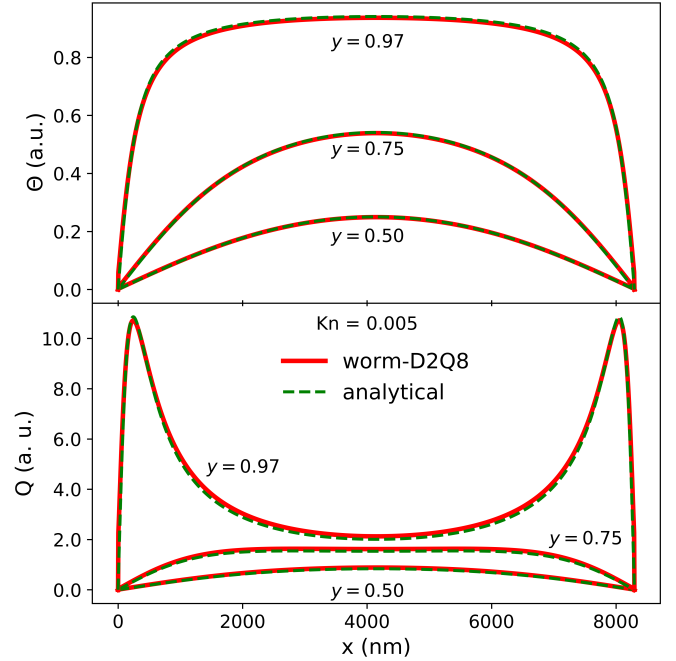


Figure 22: worm-D2Q8 steady state temperature and heat flux profiles compared to the analytical solutions (Eqs. 37 and 39). The profiles were calculated along the X directions for $Y = 0.5l_y, 0.75l_y$, and $0.97l_y$, where l_y is the length of the domain along the Y direction ($l_x = l_y = l$). A grid of $N_x \times N_y = 1598 \times 1598$ was used.

4. Conclusions

In this work, the simple and powerful worm-LBM for solving Boltzmann-type transport equations is proposed. It is an improved lattice Boltzmann method that does not suffer from the ray effect problem, which so far has rendered this method inaccurate to describe systems with high Knudsen numbers correctly (caused by a limited number of propagation directions). The worm-LBM is a simple algorithm to implement multiple propagation directions within a square scheme of the type of $\text{D2Q}[M \times 8]$ ($M \geq 1$), at the same computational cost per direction as in a standard D2Q8 scheme. The worm-LBM makes also use of an adaptive time scheme (TAS) that allows to implement isotropic as well as angular dependent propagation speeds on a regular square grid. The maximum deviation from a desired velocity and propagation direction during a worm-LBM simulation is less or equal to one grid spacing at any time. This makes the method particularly powerful for long time simulations.

The numerical accuracy of the worm-LBM algorithm was verified in the framework of thermal transport in the gray approximation. Its suitability for describing ballistic and diffusive phonon transport problems in transient and steady states was demonstrated. For the full range of Knudsen numbers and test cases, including initial and boundary conditions, the worm-LBM has shown a first-order convergence rate. The modest convergence rate is balanced by the fact that the worm-LBM already provides

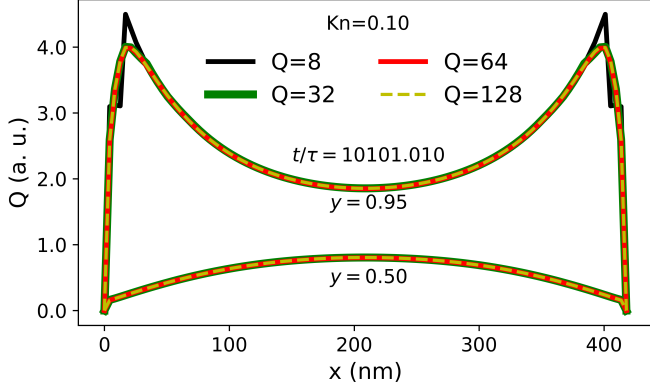


Figure 23: Q -dependence of the heat flux profile for $\text{Kn} = 0.1$. The profiles were calculated along the X directions for $Y = 0.5l_y$, $0.75l_y$, and $0.95l_y$, where l_y is the length of the domain along the Y direction ($l_x = l_y = l$). A grid of $N_x \times N_y = 98 \times 98$ was used.

accurate results with coarse grids. The largest errors are observed for the coarsest possible grid (one computational cell per mean free path) at the lowest simulated Knudsen numbers ($\text{Kn}=0.005$ - 0.01). The relative error in temperature for the cases reported at these Knudsen numbers was below 0.01 %. Conversely, for high Knudsen numbers (e.g. $\text{Kn}=20$), which imply a higher number of computational cells per mean free path, even the coarsest grid used resulted in relative errors for the temperature below 0.0001 %.

It was shown that challenging problems as the in-plane thermal transport in the ballistic regime are correctly accounted for by the new worm-LBM. The in-plane thermal transport problem, from intermediate to high Knudsen numbers, serves as a representative example of general geometries where a sufficiently high resolution in angular space is required (i.e. high number of propagation directions is needed).

The reliability of the new worm-LBM to describe phonon thermal transport, so far, has been shown in the limit of the gray approximation. Future work will involve a benchmark of the method for a full phonon dispersion, using as an input phonon properties obtained from ab initio calculations. In this regard, the algorithm has the additional advantage that different velocities can be simulated on the same grid.

Overall, due to its efficiency, simplicity, and advantages (i.e. reduced ray effect, no numerical smearing or angular false scattering), the worm-LBM has the potential of becoming the forefront methodology to tackle transport processes in a wide variety of fields.

5. Acknowledgements

The authors gratefully acknowledge the financial support under the scope of the COMET program within the K2 Center “Integrated Computational Material, Process and Product Engineering (IC-MPPE)” (Project No 859480).

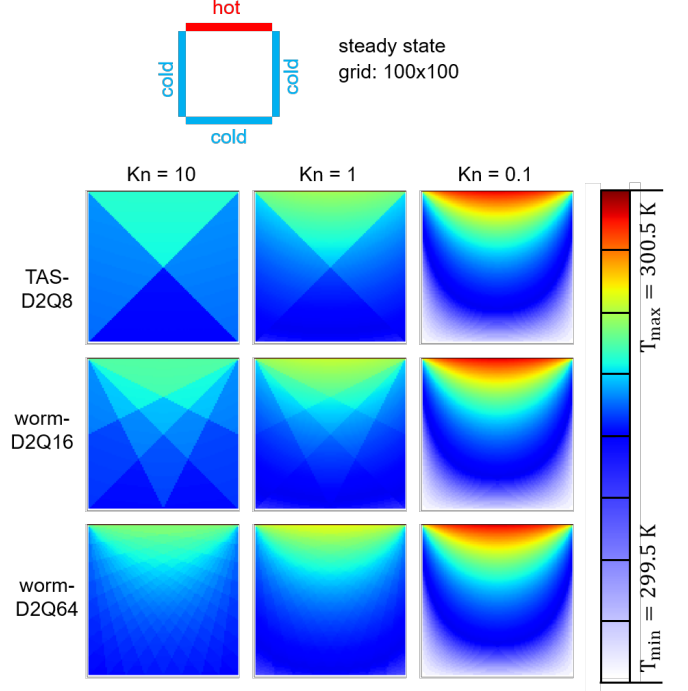


Figure 24: Steady state temperature distribution for different Knudsen numbers Kn (0.1, 1, 10), and Q directions (8, 16, 64), as calculated by different LBM schemes.

This program is supported by the Austrian Federal Ministries for Climate Action, Environment, Energy, Mobility, Innovation and Technology (BMK) and for Digital and Economic Affairs (BMDW), represented by the Austrian research funding association (FFG), and the federal states of Styria, Upper Austria and Tyrol.

6. Appendix A. Stability and dispersion relation analysis

The worm-LBM is described by linear equations (see Eq. 15). Therefore, its stability can be checked by using the von Neumann stability analysis. For simplicity we assume homogeneous W and initial conditions, which allow to write $e_i^{\text{eq}} = e_i = e(x_i)$. An algorithm is stable if the growth factor $|g| \leq 1$ for:

$$\tilde{u}^{t+\Delta t}(k) = g(k) \tilde{u}^t(k) \quad k \in \left[-\frac{\pi}{\Delta x}, \frac{\pi}{\Delta x}\right], \quad (40)$$

where $\tilde{u}(k)$ is the Fourier transform of $u(x_i) = e(x_i)$. For a step where all directions are propagating one gets:

$$\begin{aligned} \tilde{u}^{t+\Delta t} &= (1 - W)e^{ik\Delta x}\tilde{u}^t + We^{ik\Delta x}\tilde{u}^t \\ \tilde{u}^{t+\Delta t} &= e^{ik\Delta x}\tilde{u}^t \rightarrow |g| = 1, \end{aligned} \quad (41)$$

thus, this step is stable for all W . For a step where the propagation of the DDEDs is paused one obtains:

$$\tilde{u}^{t+\Delta t} = (1 - W)\tilde{u}^t + We^{ik\Delta x}\tilde{u}^t$$

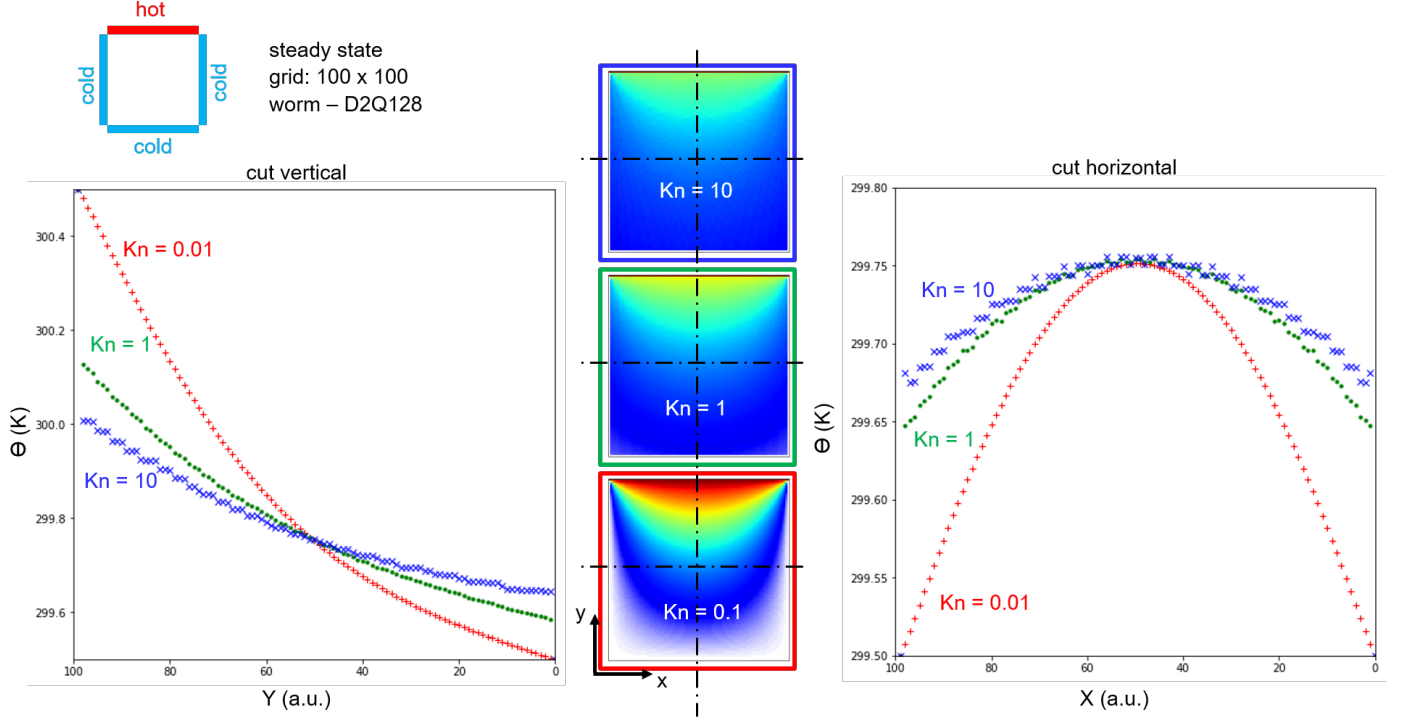


Figure 25: worm-D2Q128 steady state temperature profiles for $Kn = 0.01, 1$ and 10 . Left panel: temperature profile along the cross section at $X = 1/2$. Right panel: temperature profile along the cross section at $Y = 1/2$.

$$\tilde{u}^{t+\Delta t} = [1 + W (e^{ik\Delta x} - 1)] \tilde{u}^t. \quad (42)$$

In the limit of $W = 0$ and $W = 1$ the growth factor is exactly 1. In general, in the complex plane this result constitutes a circle with radius W , with its midpoint shifted along the real axis by $1 - W$. Therefore, the value with the highest and lowest magnitude are located on the real axis. The real part of g is:

$$\text{Re}(g) = 1 + W [\cos(k\Delta x) - 1], \quad (43)$$

showing a minimum of $1 - 2W$ and a maximum of 1. As a result the magnitude of the growth factor is smaller or equal to one for $W \leq 1$, which provides the stability limit for the scheme.

The dispersion relation is obtained by performing the Fourier transform also in time, where for the case of propagating DDESs one gets:

$$e^{i\omega\Delta t} \tilde{u} = e^{ik\Delta x} \tilde{u} \\ \omega = \frac{\Delta x}{\Delta t} k = ck, \quad (44)$$

where c is the magnitude of the lattice velocity \vec{c}_i . For steps where the DDED propagation is paused one obtains:

$$e^{i\omega\Delta t} \tilde{u} = 1 + W(e^{ik\Delta x} - 1) \tilde{u} \\ \omega = -\frac{i}{\Delta t} \ln [1 + W(e^{ik\Delta x} - 1)]. \quad (45)$$

Thus for $W = 0$ one obtains $\omega = 0$, corresponding a non-changing solution, whereas for $W = 1$ one obtains the linear dispersion $\omega = ck$.

7. References

References

- [1] P. M. Gresho, R. L. Sani., Incompressible Flow and the Finite Element Method, Volume 1: Advection-Diffusion and Isothermal Laminar Flow 1 (1998) 480.
- [2] R. E. Ewing, H. Wang, A summary of numerical methods for time-dependent advection-dominated partial differential equations, Journal of Computational and Applied Mathematics 128 (1-2) (2001) 423–445. doi:10.1016/S0377-0427(00)00522-7.
- [3] B. P. Leonard, The ULTIMATE conservative difference scheme applied to unsteady one-dimensional advection, Computer Methods in Applied Mechanics and Engineering 88 (1) (1991) 17–74. doi:10.1016/0045-7825(91)90232-U.
- [4] X. Liu, S. Zhang, H. Zhang, C. W. Shu, A new class of central compact schemes with spectral-like resolution II: Hybrid weighted nonlinear schemes, Journal of Computational Physics 284 (2015) 133–154. doi:10.1016/j.jcp.2014.12.027.
- [5] J. Hou, F. Simons, R. Hinkelmann, Improved total variation diminishing schemes for advection simulation on arbitrary grids, International Journal for Numerical Methods in Fluids 70 (3) (2012) 359–382. doi:10.1002/flid.2700.
- [6] R. Hammer, W. Pötz, A. Arnold, A dispersion and norm preserving finite difference scheme with transparent boundary conditions for the Dirac equation in (1+1)D, Journal of Computational Physics 256. doi:10.1016/j.jcp.2013.09.022.
- [7] R. Hammer, W. Pötz, A. Arnold, Single-cone real-space finite difference scheme for the time-dependent Dirac equation, Journal of Computational Physics 265. doi:10.1016/j.jcp.2014.01.028.

- [8] C. Obrecht, F. Kuznik, B. Tourancheau, J.-J. Roux, Multi-gpu implementation of the lattice boltzmann method, *Computers & Mathematics with Applications* 65 (2) (2013) 252 – 261, special Issue on Mesoscopic Methods in Engineering and Science (ICMMES-2010, Edmonton, Canada). doi:<https://doi.org/10.1016/j.camwa.2011.02.020>.
- [9] E. Calore, A. Gabbana, J. Kraus, E. Pellegrini, S. Schifano, R. Tripiccone, Massively parallel lattice-boltzmann codes on large gpu clusters, *Parallel Computing* 58 (2016) 1 – 24. doi:<https://doi.org/10.1016/j.parco.2016.08.005>.
- [10] S. Succi, *The Lattice Boltzmann Equation for Fluid Dynamics and Beyond*, Oxford University Press, 2001.
- [11] C. McHardy, T. Horneber, C. Rauh, New lattice boltzmann method for the simulation of three-dimensional radiation transfer in turbid media, *Opt. Express* 24 (15) (2016) 16999–17017. doi:[10.1364/OE.24.016999](https://doi.org/10.1364/OE.24.016999).
- [12] X. Cen, Z. Yan, J. Jiang, H. Wu, An efficient forward model based on the lattice boltzmann method for optical tomography, *Optik* 200 (2020) 163457. doi:<https://doi.org/10.1016/j.ijleo.2019.163457>.
- [13] H. Bindra, D. V. Patil, Radiative or neutron transport modeling using a lattice Boltzmann equation framework, *Physical Review E - Statistical, Nonlinear, and Soft Matter Physics* 86 (1). doi:[10.1103/PhysRevE.86.016706](https://doi.org/10.1103/PhysRevE.86.016706).
- [14] Y. Zhang, R. Qin, D. R. Emerson, Lattice Boltzmann simulation of rarefied gas flows in microchannels, *Physical Review E - Statistical, Nonlinear, and Soft Matter Physics* 71 (4) (2005) 1–4. doi:[10.1103/PhysRevE.71.047702](https://doi.org/10.1103/PhysRevE.71.047702).
- [15] X. Li, T. Ma, J. Liu, H. Zhang, Q. Wang, Pore-scale investigation of gravity effects on phase change heat transfer characteristics using lattice Boltzmann method, *Applied Energy* 222 (January) (2018) 92–103. doi:[10.1016/j.apenergy.2018.03.184](https://doi.org/10.1016/j.apenergy.2018.03.184).
- [16] Y.-L. He, Q. Liu, Q. Li, W.-Q. Tao, Lattice Boltzmann methods for single-phase and solid-liquid phase-change heat transfer in porous media: A review, *International Journal of Heat and Mass Transfer* 129 (2019) 160–197. doi:[10.1016/j.ijheatmasstransfer.2018.08.135](https://doi.org/10.1016/j.ijheatmasstransfer.2018.08.135).
- [17] S. Succi, F. Fillion-Gourdeau, S. Palpacelli, Quantum lattice Boltzmann is a quantum walk, *EPJ Quantum Technology* 2 (1) (2015) 1–17. arXiv:1504.03158, doi:[10.1140/epjqt/s40507-015-0025-1](https://doi.org/10.1140/epjqt/s40507-015-0025-1).
- [18] A. Hauser, J. L. Verhey, Comparison of the lattice-Boltzmann model with the finite-difference time-domain method for electro-dynamics, *Physical Review E* 99 (3) (2019) 033301. doi:[10.1103/PhysRevE.99.033301](https://doi.org/10.1103/PhysRevE.99.033301).
- [19] L. Zhong, S. Feng, P. Dong, S. Gao, Lattice Boltzmann schemes for the nonlinear Schrödinger equation, *Physical Review E - Statistical, Nonlinear, and Soft Matter Physics* 74 (3) (2006) 1–9. doi:[10.1103/PhysRevE.74.036704](https://doi.org/10.1103/PhysRevE.74.036704).
- [20] Z. Jiang, Z. Qu, L. Zhou, W. Tao, A microscopic investigation of ion and electron transport in lithium-ion battery porous electrodes using the lattice Boltzmann method, *Applied Energy* 194 (2017) 530–539. doi:[10.1016/j.apenergy.2016.10.125](https://doi.org/10.1016/j.apenergy.2016.10.125).
- [21] A. Chattopadhyay, A. Pattamatta, A comparative study of submicron phonon transport using the Boltzmann transport equation and the lattice Boltzmann Method, *Numerical Heat Transfer, Part B: Fundamentals* 66 (4) (2014) 360–379. doi:[10.1080/10407790.2014.915683](https://doi.org/10.1080/10407790.2014.915683).
- [22] R. A. Escobar, C. H. Amon, Thin Film Phonon Heat Conduction by the Dispersion Lattice Boltzmann Method, *Journal of Heat Transfer* 130 (9) (2008) 092402. doi:[10.1115/1.2944249](https://doi.org/10.1115/1.2944249).
- [23] Y. Guo, M. Wang, Lattice boltzmann modeling of phonon transport, *Journal of Computational Physics* 315 (2016) 1 – 15. doi:<https://doi.org/10.1016/j.jcp.2016.03.041>.
- [24] M. E. Siemens, Q. Li, R. Yang, K. A. Nelson, E. H. Anderson, M. M. Murnane, H. C. Kapteyn, Quasi-ballistic thermal transport from nanoscale interfaces observed using ultrafast coherent soft X-ray beams, *Nature Materials* 9 (1) (2010) 26–30. doi:[10.1038/NMAT2568](https://doi.org/10.1038/NMAT2568).
- [25] A. J. Minnich, G. Chen, S. Mansoor, B. S. Yilbas, Quasiballistic heat transfer studied using the frequency-dependent Boltzmann transport equation, *Physical Review B* 84 (23) (2011) 1–8. doi:[10.1103/PhysRevB.84.235207](https://doi.org/10.1103/PhysRevB.84.235207).
- [26] D. G. Cahill, P. V. Braun, G. Chen, D. R. Clarke, S. Fan, K. E. Goodson, W. P. King, G. D. Mahan, A. Majumdar, H. J. Maris, S. R. Phillpot, D. G. Cahill, P. V. Braun, G. Chen, D. R. Clarke, S. Fan, K. E. Goodson, P. Keblinski, W. P. King, G. D. Mahan, A. Majumdar, H. J. Maris, S. R. Phillpot, E. Pop, L. Shi, Nanoscale thermal transport. II. 2003–2012 011305 (January 2014). doi:[10.1063/1.4832615](https://doi.org/10.1063/1.4832615).
- [27] S. Volz, J. Ordóñez-Miranda, A. Shchepetov, M. Prunnila, J. Ahopelto, T. Pezeril, G. Vaudel, V. Gusev, P. Ruello, E. M. Weig, M. Schubert, M. Hettich, M. Grossman, T. Dekorsy, F. Alzina, B. Graczykowski, E. Chavez-Angel, J. Sebastian Reparaz, M. R. Wagner, C. M. Sotomayor-Torres, S. Xiong, S. Neogi, D. Donadio, Nanophonics: State of the art and perspectives, *European Physical Journal B* 89 (1). doi:[10.1140/epjb/e2015-60727-7](https://doi.org/10.1140/epjb/e2015-60727-7).
- [28] D. A. Broido, M. Malorny, G. Birner, N. Mingo, D. A. Stewart, Intrinsic lattice thermal conductivity of semiconductors from first principles, *Applied Physics Letters* 91 (23) (2007) 231922. doi:[10.1063/1.2822891](https://doi.org/10.1063/1.2822891).
- [29] J.-P. M. Péraud, N. G. Hadjiconstantinou, Efficient simulation of multidimensional phonon transport using energy-based variance-reduced monte carlo formulations, *Physical Review B* 84 (2011) 205331. doi:[10.1103/PhysRevB.84.205331](https://doi.org/10.1103/PhysRevB.84.205331).
- [30] B. Hunter, Z. Guo, Numerical smearing, ray effect, and angular false scattering in radiation transfer computation, *International Journal of Heat and Mass Transfer* 81 (2015) 63–74. doi:[10.1016/j.ijheatmasstransfer.2014.10.014](https://doi.org/10.1016/j.ijheatmasstransfer.2014.10.014).
- [31] R. S. Samian, A. Abbassi, J. Ghazanfarian, Transient conduction simulation of a nano-scale hotspot using finite volume lattice Boltzmann method, *International Journal of Modern Physics C* 25 (04) (2014) 1350103. doi:[10.1142/S0129183113501039](https://doi.org/10.1142/S0129183113501039).
- [32] S. Hamian, T. Yamada, M. Faghri, K. Park, Finite element analysis of transient ballistic-diffusive phonon heat transport in two-dimensional domains, *Biological Control* 80 (2015) 781–788. doi:[10.1016/j.ijheatmasstransfer.2014.09.073](https://doi.org/10.1016/j.ijheatmasstransfer.2014.09.073).
- [33] A. K. Vallabhaneni, L. Chen, M. P. Gupta, S. Kumar, Solving Nongray Boltzmann Transport Equation in Gallium Nitride, *Journal of Heat Transfer* 139 (10) (2017) 102701. doi:[10.1115/1.4036616](https://doi.org/10.1115/1.4036616).
- [34] Z. Guo, K. Xu, Discrete unified gas kinetic scheme for multiscale heat transfer based on the phonon boltzmann transport equation, *International Journal of Heat and Mass Transfer* 102 (2016) 944 – 958. doi:<https://doi.org/10.1016/j.ijheatmasstransfer.2016.06.088>.
- [35] Z. L. Guo, B. C. Shi, N. C. Wang, Fully Lagrangian and Lattice Boltzmann methods for the advection-diffusion equation, *Journal of Scientific Computing* 14 (3) (1999) 291–300. doi:[10.1023/A:1023273603637](https://doi.org/10.1023/A:1023273603637).
- [36] A. Nabovati, D. P. Sellan, C. H. Amon, On the lattice Boltzmann method for phonon transport, *Journal of Computational Physics* 230 (15) (2011) 5864–5876. doi:[10.1016/j.jcp.2011.03.061](https://doi.org/10.1016/j.jcp.2011.03.061).
- [37] S. Torquato, Y. Jiao, *Nature* 460 (7257) (2009) 876–879. arXiv:0908.4107, doi:[10.1038/nature08239](https://doi.org/10.1038/nature08239).
- [38] B. Thouy, J. P. Mazellier, J. C. Barbé, G. Le Carval, Phonon transport in electronic devices: From diffusive to ballistic regime, *International Conference on Simulation of Semiconductor Processes and Devices, SISPAD* (4) (2008) 285–288. doi:[10.1109/SISPAD.2008.4648293](https://doi.org/10.1109/SISPAD.2008.4648293).
- [39] X. Shan, X. He, Discretization of the velocity space in the solution of the boltzmann equation, *Phys. Rev. Lett.* 80 (1998) 65–68. doi:[10.1103/PhysRevLett.80.65](https://doi.org/10.1103/PhysRevLett.80.65).
- [40] N. Frapolli, S. S. Chikatamarla, I. V. Karlin, Multispeed entropic lattice boltzmann model for thermal flows, *Phys. Rev. E* 90 (2014) 043306. doi:[10.1103/PhysRevE.90.043306](https://doi.org/10.1103/PhysRevE.90.043306).
- [41] A. Fabio Di Rienzo, P. Asinari, R. Borchellini, S. C. Mishra, Improved angular discretization and error analysis of the lattice Boltzmann method for solving radiative heat transfer in

- a participating medium, *International Journal of Numerical Methods for Heat & Fluid Flow* 21 (5) (2011) 640–662. doi:10.1108/09615531111135873.
- [42] R. J. LeVeque, *Finite Volume Methods for Hyperbolic Problems*, Vol. 31, Cambridge university press, 2002. doi:10.1017/cbo9780511791253.
- [43] P. L. Bhatnagar, E. P. Gross, M. Krook, A Model for Collision Processes in Gases. I. Small Amplitude Processes in Charged and Neutral One-Component Systems, *Physical Review* 94 (3) (1954) 511–525. doi:10.1103/PhysRev.94.511.
- [44] D. P. Sellan, J. E. Turney, A. J. McGaughey, C. H. Amon, Cross-plane phonon transport in thin films, *Journal of Applied Physics* 108 (11). doi:10.1063/1.3517158.
- [45] G. Romano, A. M. Kolpak, J. Carrete, D. Broido, Parameter-free model to estimate thermal conductivity in nanostructured materials, *Physical Review B* 100 (4) (2019) 45310.
- [46] J. P. M. Péraud, *Phonon-code* (2017).
URL <https://github.com/jeanphilippeperaud/Phonon-Code>
- [47] J. E. Turney, A. J. H. McGaughey, C. H. Amon, In-plane phonon transport in thin films, *Journal of Applied Physics* 107 (2) (2010) 024317. arXiv:<https://doi.org/10.1063/1.3296394>, doi:10.1063/1.3296394.
- [48] X. Wang, B. Huang, Computational Study of In-Plane Phonon Transport in Si Thin Films , *Scientific Reports*.
- [49] S. S. Chikatamarla, I. V. Karlin, Heat equation - wikipedia, the free encyclopedia (2020).
URL https://en.wikipedia.org/w/index.php?title=Heat_equation&oldid=964338896
- [50] C. Hua, A. J. Minnich, Semi-analytical solution to the frequency-dependent boltzmann transport equation for cross-plane heat conduction in thin films, *Journal of Applied Physics* 117 (17) (2015) 175306. arXiv:<https://doi.org/10.1063/1.4919432>, doi:10.1063/1.4919432.